12-19-2003

Determination of Phase Fraction, Lattice Parameters and Crystallite Size in Mechanically Alloyed Fe-Ni Powders

Dileep Simhadri
University of New Orleans

DETERMINATION OF PHASE FRACTION, LATTICE PARAMETERS AND CRYSTALLITE SIZE IN MECHANICALLY ALLOYED Fe-Ni POWDERS

A Thesis

Submitted to the Graduate Faculty of the
University of New Orleans
in partial fulfillment of the
requirements for the degree of

Master of Science
in
Mechanical Engineering

by

Dileep Kumar Simhadri
B. Tech, Nagarjuna University

December, 2003

ACKNOWLEDGEMENTS

I would like to express my heartfelt appreciation to Dr. Paul. J. Schilling for giving me an opportunity to take up this project. His insightful analysis, wide-reaching grasp of scientific and engineering principles and passion for perfection have been a great source of inspiration.

I am grateful to Dr. Paul.D.Herrington and Dr. Melody.A.Verges for serving me on my graduate committee.

I would like to appreciate my colleagues Mr. Arun K Tatiparthi and Mr. Bhanu R Karedla for their continuous help in the lab and my friends Mr. Balakishore V Rayasam, Mr. SitaPavan Kommineni, Mr SivaRamakrishnan Sangameshwaran, Ms Sandhya Naidu Potana and my sister Ms Neelima Janyavula for their remarkable co-operation throughout the research. I would also like to thank my parents for their moral support.

DEDICATION

To my parents, who provided the inspiration and encouragement that led to my becoming an engineer, for which I will be forever grateful. They are my most ardent supporters who made me understand the learning process and taught me critical thinking skills.

Table of Contents

LIST OF FIGURES

LIST OF TABLES

ABSTRACT

This is the first systematic report on the synthesis of mechanically alloyed Fe-Ni powders ball milled at liquid nitrogen temperature. Pure Fe-Ni samples were ball milled in a SPEX 8000 shaker mill at liquid nitrogen temperature. X-ray diffractometry was used to determine the phase fractions of the bcc and fcc phases in the alloys and to determine the lattice parameters and crystallite size. The main objective of this project is to study how the milling at low temperatures affects the region of two phase co-existence, phase structure and crystallite size. It was found that the composition ranges of the bcc and fcc single phase regions were extended well beyond the equilibrium ranges. The results obtained for the samples ball milled at liquid nitrogen temperature were compared to the previous samples ball milled at room temperature.

1 INTRODUCTION

Mechanical alloying is a solid state processing technique involving repeated welding, fracturing and rewelding of powder particles in a high energy ball mill. It is non equilibrium process for material synthesis. It allows us to prepare amorphous, solid solutions, quasicrystalline and nanocrystalline structures and intermetallic phases. These mechanically alloyed powders were investigated with respect to phase formation and structure parameters such as lattice constants and crystallite size using X-ray diffraction, XANES analysis and Mossbauer spectrometry and differential scanning calorimetry (DSC). In this research Fe-Ni powders with a range of atomic compositions were ball milled at liquid nitrogen temperature. The main motive of this research is to study how milling at low temperatures affects the region of two phase coexistence between 15 and 35 at% Ni, phase structure and crystallite size. Many investigations have been carried out on Fe-Ni ball milled powders at room temperature and their thermodynamic properties and magnetic properties have been studied. This research compares the results at liquid nitrogen temperature to previous room temperature studies. Several methods have been used to investigate the changes in the ball milled powders. X-ray powder diffraction is currently used in this research.

There are two main parts in this study which involves mechanical alloying of Fe-Ni powders and X-ray powder diffraction analysis. Ball milling of Fe-Ni was carried out at low temperatures (liquid nitrogen temperature) and X-ray powder diffraction was performed on the ball milled samples. This thesis is divided into five chapters including this introduction. The second chapter is a literature review containing details about mechanical alloying, X-ray diffraction and the Fe-Ni system. A general description of mechanical alloying, its mechanism, types of mills used, important components and synthesis of non-equilibrium phases are explained. X-ray diffraction and data analysis are also explained in detail.

The third chapter deals with the experimental details including sample preparation of Fe-Ni powders using ball milling, and X-ray diffraction measurement parameters. Results are presented in chapter four. Phase fractions, lattice parameters of each phase and crystallite size of each phase were obtained from the samples milled at liquid nitrogen temperature. The results are compared to those in previous studies. Conclusions are presented in the final chapter.

2. LITERATURE REVIEW

2.1 Mechanical Alloying

Mechanical Alloying (MA) is a high energy ball milling process which produces an alloy powder by crushing / grinding two different metals together. Highly metastable materials such as intermetallic compounds, amorphous alloys and nanostructured materials can be prepared by the process. The overall composition of the particle powder which is ball milled becomes that of the average composition of the powders in the ball mill, due to the particles of different compositions adhere to each other and break away leaving traces of one particle over another. Large quantities of iron, copper, aluminum and nickel based alloys with unusual properties i.e. unusual compositions that are not possible by conventional melting technology are produced commercially using this process [Ref 1].

Originally mechanical alloying was developed around 1966 at INCO's Paul D. Merica Research Laboratory as part of a program to produce an alloy combining oxide dispersion strengthened nickel for gas turbine applications. In the early sixties INCO had developed a process for manufacturing graphic aluminum alloys by injecting nickel-coated graphite particles. A modification of the same technique was tried for nickel based alloys with a dispersion of nickel coated, fine

refractory oxide particles. The purpose of nickel coating was to make the unwetted oxide particles wettable by a nickel- chromium based alloy. Early experiments used metal-coated zirconium oxide. Analysis and mechanical property measurements revealed no differences between aluminum alloys and nickel alloys. Later it was found that they were in fact, zirconia-coated nickel rather than nickel coated zirconia [Ref 2, 3].

Oxide dispersion strengthened alloys [Ref 4, 5] were an early and obvious application of the process. Oxide dispersoids can be formed using the oxide layer common to powder particles. The particles form a metallic bond where the metal has been exposed. As the milling proceeds, the newly formed composite particles are further deformed, which causes additional breakage of the oxides. Participles will fragment resulting in composite particles. As the process continues, the size of the oxides decreases and the distribution of the oxides become more uniform throughout the powder charge.

Mechanical alloying has now been shown to synthesize variety of equilibrium and non-equilibrium alloy phases such as amorphous and nanostructured alloys [Ref 6] starting from blended elemental powders. It synthesizes materials in a non-equilibrium state by energizing. The energizing involves bringing the material into a highly metastable state by some external force e.g. melting, welding, fracture, evaporation etc. It is the result of repeated fracture and cold welding of the component particles.

The term mechanical alloying was actually given in the late 1960s by Ewan C. MacQueen, a patent attorney for the International Nickel Company (INCO). Different terms are commonly used in the literature of mechanical alloying to denote the processing of powder particles in high energy ball mills. Mechanical milling, mechanical disordering, mechanical grinding, reaction milling, cryo milling, rod milling, mechanical-activated annealing, double mechanical alloying. Milling of uniform composition powders such as pure metals or intermetallic compounds where material transfer is not required is termed as mechanical milling. During mechanical milling, the objective is to produce certain desired properties in the material, e.g., formation of nanostructured or amorphous phases or disordering of ordered intermetallics since no alloying is required to occur. Reaction milling is a mechanical alloying process accompanied by a solid state reaction. The most widely used milling now-a-days is referred as cryomilling where milling is carried out at cryogenic temperatures (very low) and in cryogenic atmosphere such as liquid nitrogen. Mechanical-activated annealing is a mechanical alloying that combines with low temperature isothermal annealing. Double mechanical alloying is a process which involves two stages where elemental powders are refined first and then subjected to a heat treatment at high temperatures.

The following sections will review the important components of the mechanical alloying process which are the raw materials, Type of mills, process control agents (PCA), process variables. [Ref 7]

2.1.1 Raw Materials

The raw materials used for mechanical alloying are widely available commercial pure metal powders that have particle size of range 1-200 μm. The critical point in mechanical alloying is that the size of the powder should be less than the ball size. This is because the size of the powder decreases exponentially with the milling time and reaches few microns. Generally used raw materials are pure metals, master alloys, prealloyed powders and refractory compounds.

2.1.2 Process Control Agents

A process control agent (PCA) is added to powder mixture during milling, when the powder mix involves a substantial fraction of a ductile component. The PCAs adsorbs on the surface of the powder particles and minimizes cold welding between powder particles and lower the surface tension of the solid material.

The PCAs are mostly organic compounds, which act as surface active agents. They are used at a level of about 1-4wt% of the total powder. Stearic acid, hexane, oxalic acid, methanol, ethanol, acetone, heptane, Nopcowax – 22DSP, octane, toluene etc are widely used. These compounds decompose during milling, interact with the powder and form compounds in the form of dispersoids inside the powder particles during milling. These are not harmful to the material, infact these contribute to dispersion strengthening of the material [Ref 8].

The choice of PCA depends on the nature of the powder being milled and the purity of the final product desired. The amount of PCA determines the final powder particle size and the powder yield.

2.1.3 Types of Mills

Different types of mills used for mechanical alloying differ in their capacity, milling efficiency and additional arrangements for heating and cooling.

2.1.3.1 SPEX shaker mills

Shaker mills are commonly used for laboratory investigations and for alloy screening purposes where 10-20g of powder can be used at a time. These mills are manufactured by SPEX CertPrep, Metuchen, N J. In this mill, vial containing the powder to be milled and the grinding balls, is clamped and swung back and forth several thousand times a minute. With each swing of the vial the balls impact against the sample and the end of the vial, both milling and mixing the sample. Majority of the research on the fundamental aspects of mechanical alloying has been carried out using some version of these SPEX mills. The ball velocities are relatively high because of the amplitude and speed of the clamp motion. Figure 2.1 shows Spex 8000 Shaker Mill.

Figure 2.1: Spex Industries 8000 Shaker Mill and Vial

2.1.3.2 Planetary Ball Mills

These mills are used, where a few hundred grams of powder can be milled at a time. It is named because of the movements of its vials as a planet. The vials are arranged on a rotating support disk where the centrifugal force produced by the vials and the rotating support disk cause both of them to rotate on their own axes. The centrifugal force acts in opposite direction which causes the grinding balls to run down the inside wall of the vial followed by the material being ground and grinding balls lifting off and colliding against the opposite side of the wall. The linear velocity of the balls are much higher than SPEX mills.

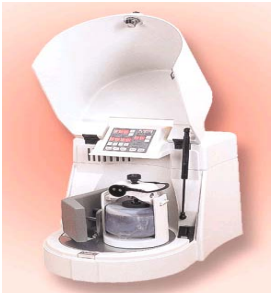

Figure 2.2: Planetary Ball Mill – Pulversitte 6

2.1.3.3 Attritor Mills

Attritors are the mills in which large quantities of the powder (from a few pounds to 100lb) can be milled at a time. The velocity of the grinding medium is much lower than in Planetary and SPEX mills. The powder to be milled is placed in a stationary tank with the grinding media. The mixture is then agitated by a shaft with arm, rotating at a high speed of about 250 rpm. This cause the media to exert both shearing and impact forces on the material. These mills work upto 10 times faster than jar mills.

Figure 2.3: Union Process 15-S Attritor

2.1.3.4 Commercial Mills

Commercial mills for mechanical alloying can process hundred pounds of powder material at a time. These mills are much larger in size than the other mills. The milling time decreases with an increase in the energy of the mill. For example, a process that takes only few mins in SPEX mill, few hours in Attritors and a few days in commercial mill.

Several new designs have been developed in recent years for specialized purposes. They are rod mills, vibrating frame mills, Uni-Ball Mill, HE mill. Some special equipment is also designed for specific laboratory applications.

2.1.4 Process Variables

We shall discuss the optimization of a number of variables required to achieve the desired product phase and/or microstructure.

2.1.4.1 Type of mill:

There are different types of mills differing in their capacity, speed of operation, ability to control temperature etc. depending on the type of powder, amount of powder required a suitable mill is selected.

2.1.4.2 Milling Container:

The materials used for the container (grinding vessel, vial, jar etc) is important as the grinding medium impacts on the wall contaminating the powder .If the same material is used, proper precautions are taken to compensate for the additional amount incorporated into the powder. Hardened steel, tool steel, hardened chromium steel, tempered steel, stainless steel, WC-Co, WC-lined steel are the most common type of materials used for grinding vessels.

2.1.4.3 Milling Speed:

The faster the mill rotates the higher the energy input into the powder. The milling speed should be just below the critical value so that the balls do not pin to

the walls and do exert some impact force. The temperature also reaches a high value yielding some advantages and also disadvantages [Ref 9]. Depending on the design of the mill some limitations are applied.

2.1.4.4 Milling time:

The time required varies depending on the type of mill, milling speed, milling temperature and ball to powder weight ratio. If the milling is done for a long time then contamination increases. Therefore it is better to mill the powder for the required duration.

2.1.4.5 Ball to powder weight ratio:

Ball to powder weight ratio (BPR) or charge ratio (CR) is an important variable in the milling process. Generally a ratio of 10:1 is commonly used for a small capacity mills and a ratio of 50:1 or 100:1 for large capacity mills. The BPR has a significant effect on the milling time. The higher the BPR, the shorter the time required to achieve a particle phase [Ref 10].

2.1.4.6 Process Control Agents (PCA):

If the powder particles are ductile they get cold welded to each other by increasing the surface tension. The PCAs reduce the cold weld and the surface tension by adsorbing on the surface. The nature and quantity of the PCA used and the type of powder determines the final size, shape and purity of the powder particles.

2.1.4.7 Milling Temperature:

Different investigations were taken into consideration to study the effect of milling temperature to determine whether an amorphous phase or a nanocrystalline structure forms and variation in solid solubility levels at different temperatures. The temperature dependence of milling-induced micro structural refinement and alloying is analyzed in terms of the dynamics of the generation and annihilation of the nonequilibrium vacancies in an externally driven system. At high temperatures the root mean square (rms) strain in the material is low and the grain size increases in nanostructures [Ref 11] and solid solubility level decreases.

2.1.5 Mechanism of Alloying

The powder particles are repeatedly crushed, grinded, fractured and rewelded during high energy ball milling. Some amount of powder is trapped in between the balls, whenever two balls collide with each other. Typically, around 1000 particles of about 0.2mg are trapped during each collision.

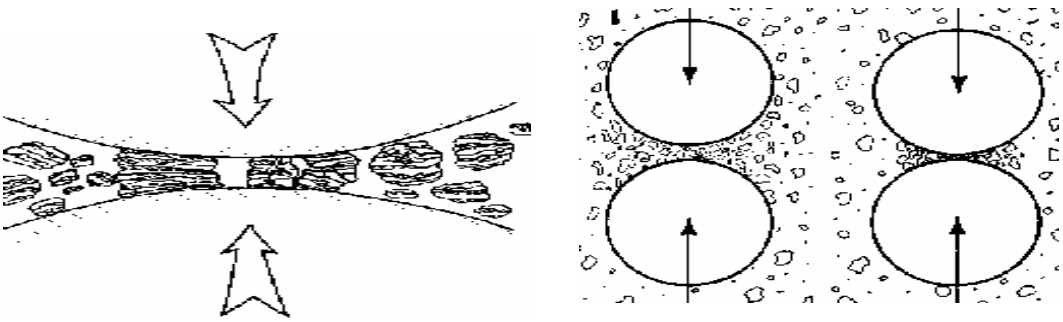

Figure 2.4: Ball-powder-ball collision of powder mixture during MA

The force of the impact plastically deforms the powder particles, creates new surfaces and enables the particles to weld together and increases the particles by size thereby. The particle size increases to as large as three times bigger than the starting particles. With the continued deformation, the particles get hardened and fracture by a fatigue failure. Fragments generated by this mechanism, continue to reduce in size in the absence of the forces. At this stage, the tendency to fracture predominates over cold welding. Due to the continuous impact of the grinding balls, the structure of the particles is steadily refined, but the particle size continues to be the same.

Because a balance is achieved between the amount of welding and the amount of fracturing, a steady state particle size distribution develops. This is the main function of mechanical alloying process conditions and the composition of alloy being processed. At this stage of processing all of lamellae within the powder particles have been reduced and the crystallite size is refined to nanometer (1nm = 10^{-9}m or 10Å). Mechanical alloying has been extensively employed to produce nanocrystalline materials [Ref 12, 13].

It is clear that during mechanical alloying, deformation occurs by the presence of a variety of crystal defects such as dislocations, vacancies, stacking faults and increased number of grain boundaries [Ref 14]. The presence of these defects increases the diffusivity of solute elements into the matrix and decreases the diffusion distances. Generally, alloying takes place at room temperature, sometimes it is

necessary to heat treat the mechanically alloyed powder for alloying to be achieved. This can be seen when formation of intermetallics is desired.

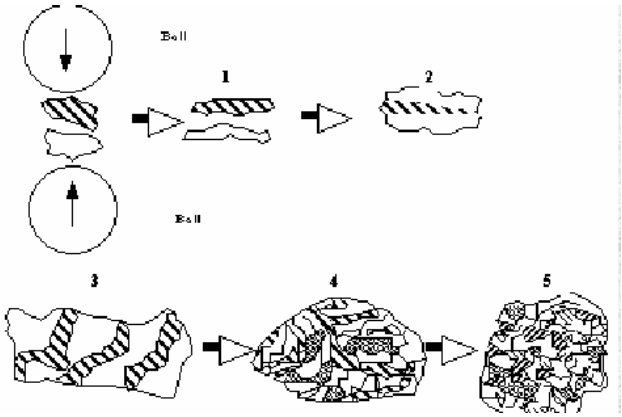

Figure 2.5: General behavior of the powder particles during mechanical alloying processing

It is possible to conduct mechanical alloying of three different combinations of metals and alloys:

(i) Ductile – ductile.

(ii) Ductile – brittle.

(iii) Brittle – brittle systems.

2.1.6 Synthesis of Non-equilibrium Phases

Mechanical alloying of suitable alloying compositions can result in the combination of variety of equilibrium, non-equilibrium phases. These include equilibrium and saturated solutions, stable and metastable crystalline intermediate phases and amorphous alloys. This technique is also capable of producing true alloys starting from pure elements that are not either easy to form or sometimes even

impossible to prepare, e.g., elements which are immiscible under equilibrium conditions [Ref 15].

Rapid solidification processing also produces very similar micro structural and constitutional effects as mechanical alloying. However, mechanical alloying process is carried out entirely in the solid state. Thus limitations imposed by phase diagrams such as immiscibility in the liquids and solid states do not apply to the mechanical alloying process. The recent advances in understanding mechanical alloying process will be discussed under the following headings:

1) Solid solubility extensions

2) Synthesis of Intermetallics

3) Disordering of ordered Intermetallics

4) Nanostructures

5) Solid state amorphization.

2.1.6.1 Solid solubility extensions

Solid solubility extensions have been achieved by mechanical alloying process and other non-equilibrium processing methods. In the early years of mechanically alloying research, observation of solid solubility extensions was not the primary objective; instead, formation of solid solutions was noted as a secondary result during amorphization of metal powder mixtures. On mechanically alloying the blended elemental powder mixtures, intermixing between the two components occurs and solid solutions can form. This solid solubility limit is expected to increase with

milling time as diffusion increases and reaches a saturation level, beyond which no further extension of solubility occurs. This can be considered as solid solubility levels achieved by mechanical alloying.

There are certain difficulties associated with the solid solubility limits determined from the changes in the lattice parameter values calculated from the shifts in the peak positions in the X-ray diffraction patterns. The absence of the second phase is usually taken as indication of formation of homogenous solid solutions. This has been proved in the Ag-Cu case, where a set of fcc peaks are shifted away from the Ag and Cu case positions, which is fairly consistent with the lattice parameters predicted by Vegard's law. Such a single set of peaks from the two constituent elements is generally regarded as indicative of homogenous supersaturation without phase separation [Ref 16].

Solid solubility extensions, beyond the equilibrium values have been reported in a number of alloy systems. It is noted that in many cases, equilibrium solid solutions (e.g., Cu-Ni, Al-Mg, and Cu-Al) were synthesized by mechanical alloying starting from blended elemental powders [Ref 17].

Equilibrium solid solubility limits are often exceeded during mechanical alloying, however no systematic study of the formation and the limits of solid solubility extensions in alloy systems by mechanical alloying have been well investigated. It was suggested [Ref 18] that the increased solid solubility of Ti in Ni mechanically alloyed Ni-Ti powder mixtures was due to the metastable equilibrium between the α-Ni solid solution and the Ni-Ti amorphous phase. The extension of

supersaturation is limited to the composition where the amorphous phase starts. A conclusion was also drawn by B.S.Murthy [Ref 19]. The extension of solid solubility was also obtained in Ni-Al and Fe-Al systems. The authors suggested that the extended solid solubility could be explained by similarity of the intermetallic and metal structures in these systems.

However, It has been noted in recent years that the solid solubility extensions can be achieved even when an amorphous phase did not form in them [Ref 20]. It was suggested that formation of supersaturated solid solutions is related to the occurrence of nanocrystalline phases. Gente [Ref 24] suggested that the increased diffusivity due to the presence of structural defects and local stress in nanocrystals is responsible for the formation of supersaturated solid solutions.

During past few years formation of supersaturated solid solutions by mechanical alloying is more noteworthy in liquid immiscible systems. A number of binary systems with positive heat of mixing have now been investigated, including Ag-Cu [Ref 21], Ag-Fe [Ref 22], Fe-Cu [Ref 23], Co-Cu [Ref 24], Cu-W [Ref 25], Cu-V [Ref 26], Cu-Ta [Ref 27], Ti-Mg [Ref 20] and Ce-Yb [Ref 28]. In most of the systems complete ranges of solid solutions are formed despite miscibility gaps in their respective equilibrium phase diagrams. Exceptions are Ag-Fe and Ti-Mg, where only little mutual solubility has been observed. There have been attempts to explain the formation of solid solution in these systems by thermodynamic arguments based on local free energy increases in the milled materials above the free energy of the solid solution [Ref 23]. A conclusion was drawn by Ma and Schilling(1997) [Ref 29] to

explain the differences in the alloying behavior between two liquid immiscible systems Ag-Fe and Cu-Fe at room temperature and intermediate temperatures. Similar conclusions were drawn by Xu explaining the differences in the alloying behavior between Ni- Ag immiscible systems [Ref 30].

2.1.6.2 Synthesis of Intermetallics:

It has been possible to synthesize a variety of intermetallic phases at appropriate compositions in a number of alloying systems because of the intimate mixing of the constituent metal powders during mechanical alloying. The intermetallics synthesized include both equilibrium and metastable crystalline phases and non-equilibrium quasicrystalline phases.

It has been reported by Eckert [Ref 31] that the nature of the phase formed in quasicrystals was different depending on the milling intensity. At very high milling intensity, a crystalline intermetallic phase formed while at very low intensity, an amorphous phase formed. A quasicrystalline phase formed at intermediate intensities. A number of intermetallics in other alloy systems have been synthesized. These include aluminides, silicides and other intermetallics. Ceramic materials such as carbides, nitrides and oxides have also been synthesized by reaction milling. In some cases, intermetallics are formed because of combustion type reactions. Ni-Al compound was synthesized this way.

Ni_3Al intermetallic powders were produced in solid state with controlled microstructure using the mechanical alloying technique by milling Ni and Al powders. In recent years ,extensive study has been carried out on the Ni-Al system [Ref 32]. It was found that mechanical alloying of Ni –Al led to the formation of metastable β' NiAl phase which reverted to the rhombohedral Ni_2Al_3 phase after annealing. Formation of a metastable phase with a simple cubic structure was also reported in mechanically alloyed Te-Ag alloys [Ref 33]. Since the powders with different compositions are impacted with high energetic balls, the process includes two simultaneous actions: cold welding between powders and fracturing of the powders. Hence, NiAl intermetallic compound with a nanocrystalline microstructure could be formed [Ref 34].

Extreme caution should be taken in identifying metastable crystalline phases produced by mechanical alloying. It is possible that some of the phases are formed due to interstitial contamination and these may be misinterpreted as new intermetallic phases.

2.1.6.3 Disordering of ordered Intermetallics:

Both ordered and disordered intermetallics have been synthesized by mechanical alloying. In some cases, the intermetallics were synthesized directly by mechanical alloying and in others a heat treatment is required. Ordered intermetallics have been found to form directly by mechanical alloying in Al-rich and Al- transition metal systems.

Reasons for the formation of ordered intermetallics are not yet studied in detail. It may be assumed that a phase can be obtained either in ordered or disordered condition depending upon the balance between atomic disordering introduced by mechanical alloying and the thermally activated reordering. The reordering is caused by the difference in energy between ordered and disordered states. Thus, if the energy is small, the alloy will be in disordered state whereas if it is large the alloy will be in the ordered state.

Disordering phenomena of ordered alloys by mechanical milling has been studied, to understand the mechanism of disordering and also to produce the disordered material that has a high deformability than the ordered alloy. A review, on this aspect has been recently published by [Ref 35]. Mechanical milling introduces high energy into the material being processed. The sum of the two effects, disordering and creation of grain boundaries will be the total energy introduced into the material by milling.

$$\Delta G \text{ (milling)} = \Delta G \text{ (disorder)} + \Delta G \text{ (grain boundaries)}.$$

Three types of transformations results during mechanical milling [Ref 35].

1. formation of solid solution e.g., Nb_3Al, V_3Ga, Ni_3Al, Fe_3Ge, Ni_2V and $NbAu_2$
2. formation of amorphous phase e.g., Nb_3Sn, NiZr, NiV_2, CoZr and
3. formation of a different phase with a complex crystal structure, e.g., Ni_3Sn_2, $TiSi_2$

According to Miedema analysis introduced by Bakker, if ΔG (milling)> ΔG (disorder-grain boundaries) complete amorphization occurs. On the other hand, if ΔG (milling) < ΔG (disorder-grain boundaries), solid solution occurs.

During disordering of CoZr, It was observed [Ref 36] that there is no decrease in the intensity of superlattice reflections with milling time and the magnetization in Co-Zr alloys increases continuously and also the lattice parameter of the disordered nanocrystalline phase increased with milling time. From the above observations, it was concluded that disordering of CoZr occurs by atomic disorder and grain refinement.

The magnetic measurements are very powerful in determining the nature of disordering if one of the atoms involved has magnetic moments. There has been a great interest recently on the study, performed on order-disorder and magnetic properties of mechanical alloyed nanocrystalline Ni_3Al alloy [Ref 37].

Upon continuous milling, the long range order parameter, S in the intermetallic is gradually reduced. The material becomes totally disordered, if S=0, e.g., Ni_3AL [Ref 38] and in some cases partial order and partial disorder coexist if S is reduced and $S \neq 0$ e.g., CuTi [Ref 39]. In some other cases, the value of S does not reduce at all and S=1 and becomes amorphous e.g., CoZr [Ref 36]. Thus upon milling, an ordered intermetallic can transform into disordered crystalline phase (solid solution) or an amorphous phase.

2.1.6.4 Nanocrystalline materials:

Nanocrystalline materials have been synthesized by a number of techniques starting from vapor phase (inert gas–condensation), liquid phase (electrodeposition and rapid solidification) and solid state (mechanical attrition). The

ability to produce bulk quantities of material in the solid state using simple equipment and at room temperature is the main advantage of mechanical alloying for synthesis of nanocrystalline materials.

The first report of formation of a nanostructure material synthesized by mechanical alloying is by Thompson and Politis in 1987. The specific mention of formation of "nanometer order crystalline structures" was by Shingu. Koch [Ref 12] has summarized the results on the synthesis and structure of nanocrystalline structures. In almost all mechanically alloyed pure metals, intermetallics and alloys, it has been observed that the grain sizes are of nanometer dimensions. Hellstern [Ref 9] have described the mechanism of formation of structures. Plastic deformation by ball milling occurs due to shear bands which are 0.5μm wide. In the early stages plastic strain in the material increases due to the increasing dislocation density and the crystal disintegrates into subgrains that are separated by low angle grain boundaries. During subsequent milling high deformation / subgrain formation is repeated resulting in subgrains becoming finer and finer and the orientation becoming completely random. Once the critical level of refinement is reached, further refinement becomes impossible because of the stresses being high for dislocation movement. Thus nanostructures of minimum grain size are produced [Ref 40].

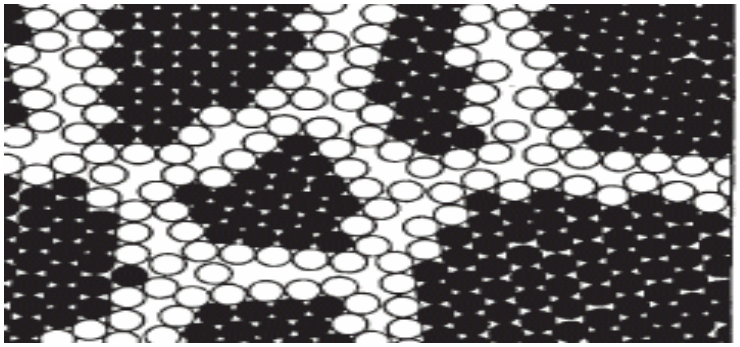

Figure 2.6: 2-D Model of Nano Crystalline Material (Gleiter 1996, 2000)

Nanostructure processing leads to the formation of supersaturation solid solutions and intermetallic compounds. If the grain size is in the nanometer range a homogenous supersaturated solid solution can be obtained in the system [Ref 24]. The large volume fraction of grain boundaries in these materials is expected to enhance the diffusion and consequently extend the solid solubility levels in these types of systems. Similarly formation intermetallics such as Pd_3Bi and CuEr has been achieved by nanostructure processing.

2.1.6.5 Solid-state Amorphization:

Amorphous phases are formed by different processing techniques in liquid and vapor state. The change in the state of matter i.e., solid phase is formed from either the liquid phase or the vapor phase have been shown to be responsible for the amorphization process. There are also methods of amorphizing a solid without passing through the liquid or vapor stage known as solid-state amorphization.

Amorphous phase formation is the most widely studied aspect of mechanical alloying as it is the simplest of all solid state amorphization techniques.

Weeber and Bakker [Ref 41] reviewed the experimental evidence for amorphization by high energy ball milling. The process may be classified into two categories which increased the research activity in this area. First, synthesis of Ni-Nb amorphous phase from blended elemental powders of Ni and Nb by mechanical alloying [Ref 42] and second, amorphization of intermetallic compounds by mechanical milling.

The process of amorphization of elemental powders has been explained by Schwarz and Johnson [Ref 43] and Hellstern [Ref 44] as the synthesis of an ultrafine composite in which solid state amorphization takes place. The formation requires that the powders (i) have a large negative heat of mixing in the amorphous state and (ii) have very different atomic sizes, allowing one component to diffuse more rapidly than the other. The negative heat of mixing provides the driving force for the reaction and the large difference in the diffusivities is necessary for the kinetics of the reaction. These factors explain the formation of amorphous phase by mechanical alloying of a mixture of pure components.

The case of amorphization of an intermediate phase by mechanical milling was first observed by Ermakov. Here the starting material is the equilibrium phase. The free energy of the equilibrium crystalline intermediate phase must be raise above that of the amorphous phase. The increase of free energy is due to the defects introduced by the plastic deformation.

A large number of binary metal (TM_1) – metal (TM_2) alloys have been observed to form amorphous phases by mechanical alloying using the elemental powders where TM1 is Cr, Mn, Fe, Co, Ni, Cu, Pd or Ru and Tm2 is Zr, Ti, Nb or Hf

[Ref 43, 44]. A schematic study of glass forming ability has been performed for transition metal alloys with Ti-Ni-Cu & Al-Ti [Ref 45], Ti-Mn & Ti-Fe [Ref 46] and with Zr –V & Zr-Co [Ref 47].The structure of amorphous binary metal-metal alloys produced by mechanical alloying have been evaluated by Christian and his co-workers [Ref 48].

2.2 Fe-Ni system:

Fe-Ni system has attracted considerable attention as a basis for a number of alloys with special magnetic and mechanical properties. Severe plastic deformation of these alloys in various kinds of high-energy mechanoactivators enables one to obtain alloys with new structures and properties. Therefore, several studies were performed, where structure and magnetic properties of mechanically alloyed (MA) Fe-Ni alloys were investigated [Ref 49-54]. Recent studies of mechanical alloyed binary alloys showed that the single phase concentration region extend significantly as compared with those for alloys produced by conventional techniques. For the Fe-Ni also this tendency takes place but the results obtained by different researchers although similar in general do not coincide completely [Ref 49, 52].

During the past few years the formation of supersaturated solutions in Fe-Ni systems has received increased attention. Since the Fe-Ni system has small negative heat of mixing mechanical alloying of Fe-Ni results in the formation of solid solutions than in amorphization [Ref 53]. In the equilibrium phase diagram, Fe and Ni

are immiscible in both the solid and liquid states. A steady of thermal stability shows that milling at high temperatures leads to lower solubility.

It was observed that the concentration ranges of the bcc and fcc single phase solid solution depend on the milling intensity and shift to low Ni rich concentration at an increase in the milling intensity. Some peculiarities of phase transformation in Fe-Ni alloys is obtained. Annealing of mechanical alloys leads to further extension of fcc single-phase concentration range. This is obtained after the austenite-martensite phase transformation is formed by different treatments such as cooling. For comparisons, the compositions of bcc and fcc phases at various temperatures determined by magnetic methods to represent equilibrium states are given.

From the technical point of view, the metastable states occurring in the Fe-rich alloys are of much importance. The fact that the bcc to fcc transformation is affected with a temperature hysteresis that increases with increasing Ni content shows the existence of metastable conditions. The mode and rate of the transformations occurring after various pre-treatments is not understood.

Many investigations were carried out to study the magnetic behaviour of Fe-Ni system because of its magnetic materials ranging from high permeabilities of soft magnetic alloys to high coercivity permanent magnetic alloys. It has been shown for mechanically alloyed Fe-Ni alloys, that a nanocrystalline state improves subsantially the soft magnetic properties[Ref 55]. In this systems disordered solid solutions were formed by the measurement of saturation magnetization. The soft

magnetic behaviour of the material shows some features of rapidly quenched nanocrystalline structures but very low coercivities are prevented by strain through magneto-elastic interaction.

2.3 X-ray Powder Diffraction:

Following the discovery of x-rays by German physicist W C Roentgen in 1895, three major branches of science have developed from the use of this radiation. The first and the oldest is x-ray radiography, which makes the fact that the relative absorption of x-rays by matter is a function of the average atomic number and the density. Early attempts to confirm the dual nature of x-rays, i.e., their particle and wave character were frustrated by experimental difficulties involved with the very short wavelengths. It was not until the classic work of Max Von Laue 1912, that the exact nature of x-rays was confirmed by diffraction experiments from a single crystal. Radiography is limited to sizes of order 10-1 cm where as, diffraction can reveal the details of the internal structure of the order of 10-8 cm in size. The third technique, x-ray spectrometry which has the same fundamentals was developed over last 20-30yrs [Ref 56].

2.3.1 Origin of X-radiation:

We know that x-rays are relatively short-wavelength, high energy beams of electromagnetic radiation. When an x-ray beam is viewed, it appears as a sinusoidal oscillating electric field, at right angles to it, similarly varying magnetic

field changing with time or sometimes referred as particles of energy called photons. Therefore all electromagnetic radiations are characterized either by its wave character using wavelength λ or its frequency ν or by means of its photon energy E.The following equations represent the relationships between them:

$$E = h\nu \ , \qquad \nu = \frac{c}{\lambda},$$

were *c* is velocity of light and *h* is Planck's constant. From both the equations, the energy of X-ray photon is

$$E = \frac{hc}{\lambda} \text{----------(1)}$$

The x-ray region normally considered is between 0.1 and 100Å (1Å = 10^{-10} cm) and in terms of energy covers 0.1 to 100keV. Inserting appropriate fundamental constants gives

$$\mathbf{E} = \frac{12.398}{\lambda}$$

as an example the Cu $K\alpha_1$, $K\alpha_2$ has an energy of 8.06 keV, corresponding to a wavelength of 1.51 Å.

2.3.2 Production of X-rays:

X-rays are produced in a highly evacuated glass bulb, called an x-ray tube that contains essentially two electrodes—an anode made of platinum, tungsten, or another heavy metal of high melting point, and a cathode. When a high voltage is

applied between the electrodes, streams of electrons (cathode rays) are accelerated from the cathode to the anode and produce x-rays as they strike the anode.

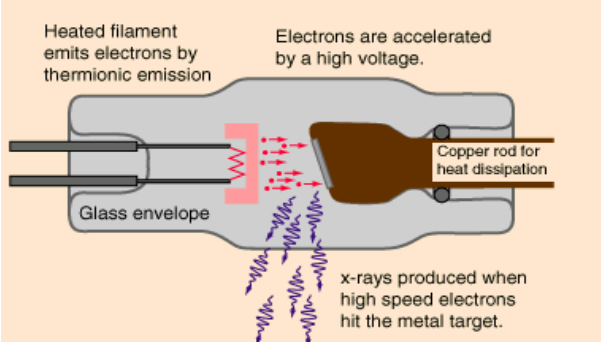

Figure 2.7: X-ray Tube

X-rays are produced when high energy electrons collide with a metal target, interacting with its atoms. The potential difference (pd) across the x-ray tube accelerates the electrons from the cathode to the anode, increasing their kinetic energy (KE). Two different processes give rise to radiation of x-ray frequency. In one process radiation is emitted by the high-speed electrons themselves as they are slowed or even stopped in passing near the positively charged nuclei of the anode material. This radiation is often called brehmsstrahlung [braking radiation]. In a second process radiation is emitted by the electrons of the anode atoms when incoming electrons from the cathode knock electrons near the nuclei out of orbit and they are replaced by other electrons from outer orbits. The spectrum of frequencies given off with any particular anode material thus consists of a continuous range of frequencies emitted in the first process, and superimposed on it a number of sharp peaks of intensity corresponding to discrete frequencies at which x-rays are emitted in the second process. The sharp

peaks constitute the x-ray line spectrum for the anode material and will differ for different materials [Ref 57].

Characteristic x-rays are emitted from heavy elements when their electrons make transitions between the lower atomic energy levels. The characteristic x-rays emission which shown as two sharp peaks in the illustration below occur when vacancies are produced in the n=1 or K-shell of the atom and electrons drop down from above to fill the gap. The x-rays produced by transitions from the n=2 to n=1 levels are called K-alpha x-rays, and those for the n=3->1 transition are called K-beta x-rays. Transitions to the n=2 or L-shell are designated as L x-rays (n=3->2 is L-alpha, n=4->2 is L-beta, etc.)

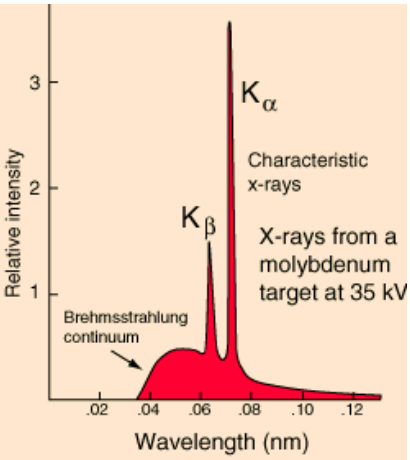

Figure 2.8: X-ray Characteristics

2.3.3 Diffraction of X-rays:

The oscillating electric field of a light wave will interact with the electrons in the matter to cause coherent scattering. The waves scattering from two

objects will expand in space around the objects until they interfere with each other. Their interaction will produce constructive interference at certain angles and destructive interference at other angles. When a periodic array of objects each scatters radiation coherently, the constructive interference at specific angles is called diffraction.

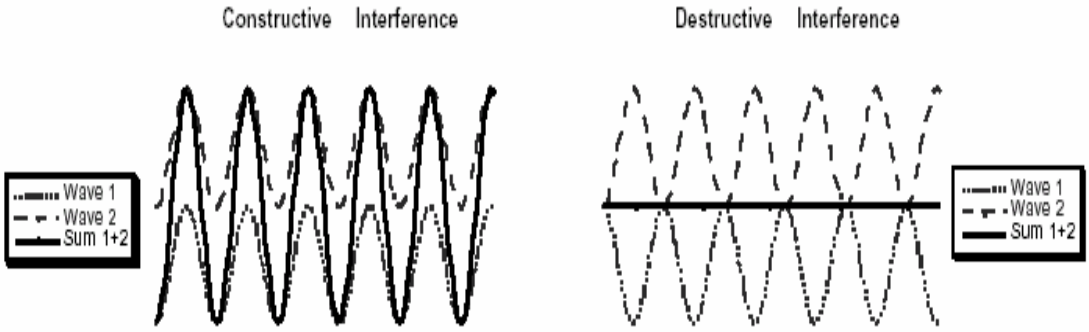

Figure 2.9: Constructive and Destructive Interference scattering waves

The first description of the diffraction of X-rays by a crystal was developed by Max Von Laue. In 1913, William Henry Bragg and his son William Lawrence Bragg developed a much simpler way of understanding and predicting diffraction phenomena from a crystal. Consider first a single plane of regularly spaced atoms. Imagine a beam of coherent light is incident on the atoms at an angle θIN. Some of the rays interact with the atoms and are scattered in all directions. (Most of the rays are transmitted) [Ref 58].

Consider the two scattered waves, A and B. They are in phase, reinforcing each other to give a diffracted beam, only when they travel the same

distance, i.e. when x = y. This only occurs for scattered waves with an outgoing angle of:

$$\theta_{OUT} = \theta_{IN} = \theta$$

Thus a diffracted beam from a single row of atoms is made up of all the waves which are scattered with an outgoing angle equal to the incoming angle of the incident waves. This is true for incident waves of any wavelength. The two waves A and B, scattered from particles in adjacent planes are separated by a distance d. They are only in phase if the extra path length of wave B over A (= x + y) equals a whole number of wavelengths.

The equation for this path difference gives the Bragg law:

$$x + y = 2d\sin\theta = n\lambda$$

This condition which gives rise to diffracted beams depends on the wavelength, l; the spacing of the planes of atoms, d; and the angle of incidence of the beam, θ. This condition is known as Bragg's law: the great law of scattering and diffraction

$$n\lambda = 2d\sin\theta \text{ ----------(2)}$$

For a particular pair of *d* and λ values there may be several values of θ at which diffraction occurs. To use the Bragg Law, two things are worth remembering:

- the incident beam, the normal to the reflecting plane and the diffracted beam always are coplanar.
- the angle between the transmitted beam (the incident beam propagating through the scattering material) and the reflected beam is 2θ.

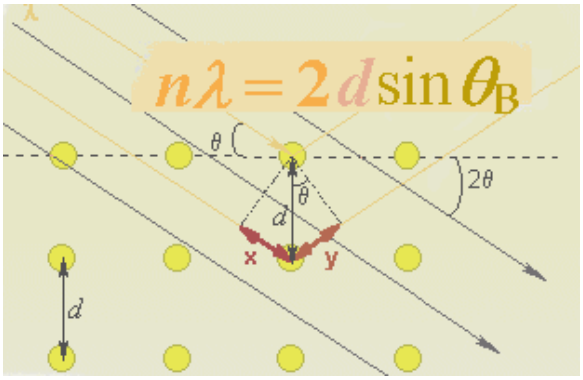

Figure 2.10: Geometry of Diffraction

2.3.3.1 Reciprocal Lattice:

It is difficult to imagine how a beam of waves entering a crystal might be diffracted with so many different planes set at different angles to the beam, all with different spacings. Which, if any of these planes will satisfy the Bragg law? To help us we use the idea of reciprocal lattices developed by P.P.Ewald.

A reciprocal lattice is a construction drawn in reciprocal space, where we use reciprocal space. A dimension of 1/*d*, where *d* is the spacing between crystal planes, is frequently used. Consider a beam of waves to be incident on a crystal. The measurement, *r*, made from the diffraction pattern, tells us about 2θB. From this we can deduce 1/*d*, since we know that for diffraction of radiation of wavelength, λ, the Bragg angle, θB, increases with 1/*d*.

For example, if the crystal is cubic, then

$$\frac{1}{d} = \frac{\sqrt{h^2 + k^2 + l^2}}{a} \text{----------(3)}$$

We use the notation (*hkl*) to designate planes in a real lattice. In a reciprocal lattice, the reciprocal lattice points (relpoints) are labeled (or indexed) the same, since they represent the planes in the real lattice. Peter Ewald published details of a geometrical construction which has been used ever since for interpreting diffraction patterns. When a beam hits a crystal, Ewald's sphere shows which sets of planes are at (or close to) their Bragg angle for diffraction to occur [Ref 59].

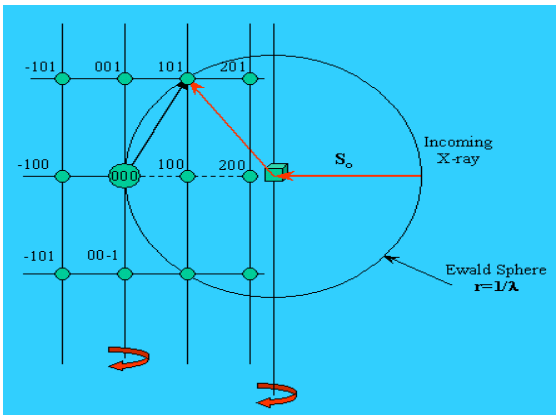

Figure 2.11: Ewald Sphere: radius determined by wavelength, 1/λ

2.3.4. Diffraction Methods:

For a single crystal, a single wavelength and a single orientation of the crystal to the main beam it is unlikely that the Bragg condition will be met for a given plane. Rotation of the crystal will bring planes into the Bragg condition. This means that it is desirable to have one of these parameters have variability. X-ray spectrometer method in which rotation of a perfect crystal in an x-ray beam is one method to determine the x-ray spectrum using Bragg's Law. In a Laue camera, a polychromatic

incident beam many planes will meet the Bragg condition and tracing the 2-d pattern on a photographic film will reveal the planes of a zone. There are two practical variants of the Laue method, the back-reflection and the transmission Laue method. We can perform this experiment in lab. In the rotating crystal method, a single crystal is mounted with an axis normal to a monochromatic x-ray beam. A cylindrical film is placed around it and the crystal is rotated about the chosen axis. As the crystal rotates, sets of lattice planes will at some point make the correct Bragg angle for the monochromatic incident beam, and at that point a diffracted beam will be formed.

Powder diffraction method was used in this research. Used for a monochromatic beam, polycrystalline sample and is usually done with a flat film in pinhole arrangement. The diffractometer method is similar to the powder method but uses a step-scanner and a line beam. Usually involves a polycrystalline sample.

2.3.5 Intensity of Diffraction:

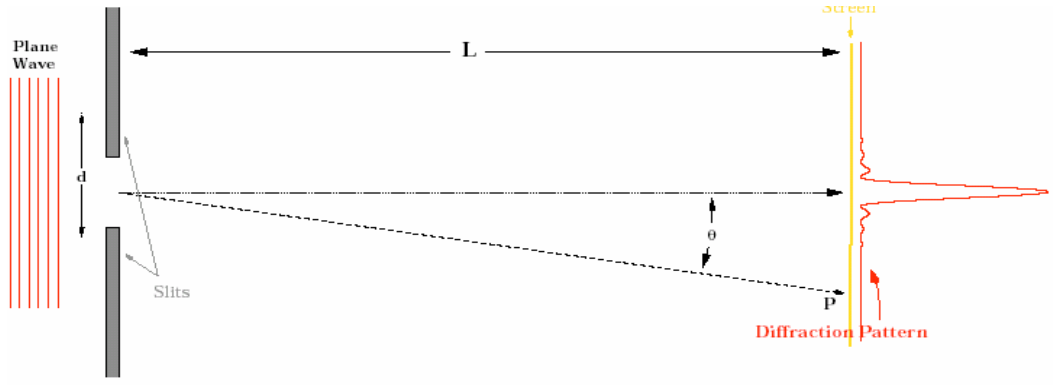

Figure 2.12: Intensity Profile of a Diffraction Pattern

The positions of the atoms in the unit cell will affect the intensities, but not the positions of the diffracted beams. By studying the intensities of the beams, it is possible to say something about the atomic arrangements within the unit cell.

2.3.5.1. Scattering of x-rays by an electron :

When electrons find themselves in and electromagnetic field, they respond to the electric part of it by oscillating with the same frequency thereby emitting electromagnetic waves in all directions. The sum of the emissions of all the radiated electron make up the scattered beam. There is a phase change of λ/2 associated with the scattering though the frequency of the scattered (or diffracted) beam is the same as for the incident beam, but as this phase change is the same for every scattered photon, it doesn't matter in the derivation of Bragg's law.

Though an electron scatters an incident beam in all directions, it doesn't emit equal amount of radiation in all directions. J. J. Thompson found a formula, that describes the intensity I of a beam scattered by a single electron of charge e (in Coulombs) and mass m (in kg.), at a distance r meters from the electron, where α is the angle between the scattering direction and the direction of acceleration of the electron:

$$I = I_0 \left(\frac{\mu_0}{4\pi}\right)^2 \left(\frac{e^4}{m^2 r^2}\right) \sin^2 \alpha \quad \text{----------} \quad (4)$$

2.3.5.2 Scattering of x-rays by an atom :

In an atom all electrons would contribute to scattering, whereas the nucleus is too heavy to accelerate and scatter. As the electrons are positioned differently around the nucleus their scattered waves differ somewhat in phase (except from scattering in the forward direction). The net scattering from an atom is therefore not just the added amplitudes, but less than this. To describe the efficiency of a given atom to scatter in a given direction, the atomic scattering factor, f, is introduced:

f = amplitude of the wave scattered by an atom / amplitude of the wave scattered by one electron.

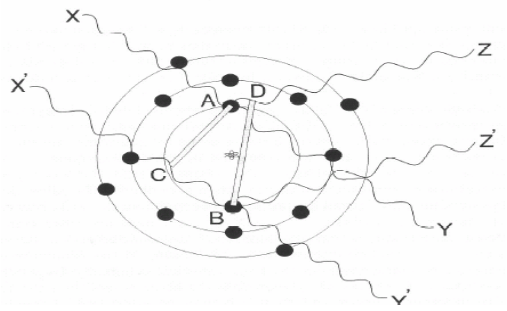

Figure 2.13: The Scattering of X-rays from a real atom extended in space

Since the intensity is the amplitude squared, the intensity can be found from a curve of f versus $\sin\theta$.

2.3.5.3 Scattering of x-rays by a unit cell :

As it was the case with the different electrons in one atom, so it is the case with the different atoms in a unit cell: The scattered rays from each atom in the

cell will not necessarily be in phase except in the forward scattering direction. The effect of that is expressed via the structure factor F:

$$F_{hkl} = \sum_1^N f_n e^{2\pi i(hu_n + kv_n + lw_n)} \quad \text{----------} \quad (5)$$

Where N is the number of atoms in the unit cell and (u v w) are their fractional position within the unit cell. Thus it is possible to calculate the intensities of all reflections, h k l [Ref 60, 61, 62].

2.3.6. Factors affecting the Diffraction Intensities :

By considering all of the factors affecting the relative intensity diffractions produced by the lattice planes of a crystal structure, it is possible to calculate a theoretical diffraction pattern for virtually any crystalline material. We will not actually do these calculations, but it is important to be aware of these factors when you interpret your data.The factors are summarized in the following sections [Ref 60].

2.3.6.1 Multiplicity Factor :

The number of planes cutting a unit cell in a particular hkl family is called the plane multiplicity factor. For example ,in a cubic crystal there will be 111 ((1 1 1), (1 1 -1), (1 -1 -1) and (1 -1 1)) and 101((0 0 1), (0 1 0) and (1 0 0)) planes having same lattice but different orientations. As there are more [1 1 1] planes than [1 0 0] planes, the intensity of the [1 1 1] beam should be 4/3 of the intensity of the [1 0 0] beam. This is called the multiplicity factor.

2.3.6.2 Polarization Factor :

The incident X-ray beam is unpolarized and the process of scattering polarizes it resulting in a directional variation in the scattered intensity. Thus an additional factor is seen in the all the intensity equations.This is called polarization factor.

$$PF = \frac{1+\cos^2 2\theta}{2} \text{----------(6)}$$

2.3.6.3 The Lorentz Factor :

When each lattice point on the reciprocal lattice intersects the diffractometer circle, a diffraction related to the plane represented will occur. The diffractometer typically moves at a constant 2θ rate. As angles increase, the intersection approaches a tangent to the circle; thus at higher angles, more time is spent in the diffracting condition. This may be corrected by inserting the term I/(sin2θ cosθ) into the expression for calculating diffraction intensities; this is called the Lorentz factor.

$$Lorentzfactor = \frac{1}{4\sin^2\theta\cos\theta} \text{---------(7)}$$

In practice, this is usually combined with the atomic scattering polarization term (Thompson equation) and called the *Lorentz polarization (Lp) correction*.

$$Lorentz-polarizationfactor = \frac{1+\cos^2 2\theta}{\sin^2\theta\cos\theta} \text{--------(8)}$$

2.3.6.4 Extinction Factor :

In addition to systematic extinctions related to crystal structure, another extinction phenomenon can occur which is related to a phase-shifted reflection which can occur from the underside of very strongly reflecting planes. Directed towards the incident beam but always 180° out of phase with it, the net effect is to reduce the intensity of the incident beam, and secondarily the intensity of the diffraction from that plane.

2.3.6.5 Absorption Factor :

Absorption occurs related to the area of a powder specimen and depth of penetration of the x-ray beam into the specimen. In general, the larger area of sample irradiated at low 2θ values have less depth of penetration. At higher 2θ values, the irradiated area will smaller, but depth of penetration greater. In general, these tend to be offsetting effects as related to diffracted intensity over the angular range of the data collection. The calculated intensity will include a term for 1/μs where μs is the linear absorption coefficient of the specimen.

2.3.6.6 Microabsorption Factor:

Microabsorption is a phenomenon that occurs in polyphase samples. Typically the linear absorption coefficient is calculated based on the proportions of the phases in the mixture. Microabsorption occurs when large crystals preferentially interact with the beam causing both anomalous absorption and intensities not representative of the proportions of the phases. The effect is minimized in diffraction experiments by decreasing the crystallite size in the specimen.

2.3.6.7 Monochromator Polarization :

As the diffracted beam is partially polarized by the diffraction process, a crystal monochromator adds another diffraction to the diffracted beam, thus a term related to the diffraction angle of the monochromator (θm) is added to the (Lp) correction. It should be noted that for pyrolitic graphite (PG) monochromators, the curved crystal geometry tends to minimize the intensity loss due to the polarization effect such that the correction term tends to over estimate the intensity loss.

$$MP = \frac{1+\cos^2 2\theta \cos^2 2\theta_m}{2} \text{----------(9)}$$

2.3.7 The Intensity Equation :

All the factors affecting the intensity of a diffraction peak may be summarized in the following equations. The calculation is done regularly to produce the "calculated patterns" in the ICDD Powder Diffraction File database. The Intensity of diffraction peak from a flat rectangular sample of phase α in a diffractometer with a fixed receiving slit (neglecting air absorption), may be described as:

$$I = |F|^2 p(\frac{1+\cos^2 2\theta}{\sin^2 \theta \cos\theta}) \text{----------(10)}$$

The relative intensity is converted to a normalized scale by dividing by the brightest peak intensity and multiplying by 10 or 100 to get the results on a percent of brightest peak scale for instance.

2.3.8 Crystallite Size:

For crystallites of large size (i.e., thousands of unit cells), the nature diffraction will produce diffraction peaks only at the precise location of the Bragg angle. If the particle size is smaller the net result will be a broadening of the diffraction peak around the Bragg angle. This phenomenon of widening of diffraction peaks is related to incomplete "canceling" of small deviations from the Bragg angle in small crystallites is known as particle size broadening. Particle size broadening is differentiated from the normal width of diffraction peaks related to instrumental effects. The crystallite size broadening βτ of a peak can usually be related to the mean crystallite dimension (τ) by the Scherrer equation:

$$\tau = \frac{k\lambda}{\beta_\tau \cos\theta} \text{----------(11)}$$

where β_τ is the line broadening due to the effect of small crystallites: $\beta_\tau = B - b$.

B, being the breadth of the observed diffraction line at its half-intensity maximum, and b, the instrumental broadening and K is the shape factor = 0.9 . The general relation is shown in the Figure.

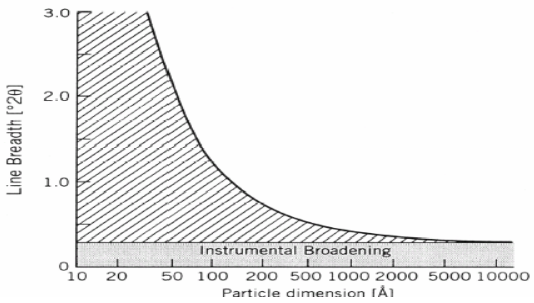

Figure 2.15: Line Width as a function of particle dimension

Various methods are employed to calculate the average crystallite size and average lattice strain. Integral breadth method and Fourier methods are generally used to calculate the sources of peak broadening.

2.3.8.1 Integral Breadth methods :

Integral breadth, β is the peak area divided by the peak maximum. It is the width of a rectangle with the same area and height as the peak concerned. If the integral breadth of an observed peak profile could be seen only due to the size broadening, the volume average crystallite size L would be:

$$L_{hkl} = \frac{K\lambda}{\beta \cos\theta} \text{----------(12)}$$

This is known as Scherrer's equation, where **K** is a Scherrer constant with a value 1.0≥K≥0.9, **λ** is X-ray wavelength, **θ** is diffraction angle and **β** is integral breadth(in radians).If the integral breadth of an observed peak profile could be seen only due to lattice distortions, then mean lattice strain ***e*** would be :

$$e_{hkl} = \frac{\beta}{4 \tan\theta} \text{----------(13)}$$

2.3.8.2 Williamson – Hall Method :

Williamson and hall proposed this method of interpreting particle size broadening and strain broadening. This method is due to the instrumental broadening. All the peaks in the diffraction pattern can be used for the calculation of size and strain. This method consists essentially plotting between βCosθ and Sinθ. The grain size is obtained from the extrapolated y- intercept and the root-mean squared strain from the slope of the plot.

$$\beta \text{ (sample)} = \beta \text{ (size)} + \beta \text{ (strain)}$$

$$\beta = \frac{1}{L\cos\theta} + 4e\tan\theta$$

$$\beta\cos\theta = \frac{\lambda}{L} + 4e\sin\theta \text{ ----------} (14)$$

In order for the peak widths to linearly combine a Lorentzian peak profile is necessary. Gaussian peaks add together as squares {β2 (sample) = β2 (size) + β2 (strain)}. Investigators used different methods to calculate the crystallite size. Hong and Fultz [Ref 49] obtained the grain size using Williamson and Hall [Ref 51] method and Scherrer equation considering FWHM of a Lorentzian fit to the diffraction peak.

3. EXPERIMENTAL DETAILS :

3.1 Sample Preparation:

Elemental powders of Fe (particle size : -325 mesh) and Ni (particle size : -100 mesh) with nominal purity of 99.9 wt% were used as starting materials. Ball milling was performed in a SPEX 8000 shaker mill. The powders were mixed to give the desired average composition and the powder blends were sealed with hardened steel balls in a hardened steel vial under a purified argon atmosphere to minimize the gaseous contamination from the air. No process control agent was added to minimize the potential contamination. The ball to powder weight ratio was about 5:1. Ball milling was performed at LN2T (-196°C) by continously dripping liquid nitrogen into a ploystyrene foam container surrounding the outside of the vial. The powders were milled for 12 hrs. After milling the vials were warmed back to RT to avoid contamination from condensation before opening.

For the calibration purpose pure Fe and Ni powders of 99.9% purity were taken and mixed together to obtain the desired compositions. Taking the at% of the milled powders, wt% is calculated and the exact amount of powders are mixed and the desired compositions are obtained. X-ray diffractometry was performed on

standard powders with Philips X'Pert Diffractometer and Cu Kα incident radiation at room temperature.

3.2 Introduction to the X-Pert Pro System :

This section gives the details of the X'pert Pro system used in the research and the details are obtained from the system manual [Ref 63].

Figure 3.1: PW 3040/60 X'Pert Pro X-ray Diffraction System

The Philips X'Pert PRO x-ray diffraction system is the basic platform for a wide variety of application in analytical x-ray diffraction.

The following applications are possible with X'Pert diffractometer:

- High resolution rocking curve analysis, reciprocal space mapping and x-ray topography on (epitaxial) layers on single crystal substrates.

- Reflectometry on thin layers and substrate materials.
- Analysis of small spots on inhomogeneous samples.
- Phase analysis of samples with flat or irregular surfaces of thin films and of samples in glass capillaries.
- Crystallography and Rietveld analysis on samples with flat or irregular surfaces or powder samples in glass capillaries.
- Residual stress analysis of flat samples or irregularly shaped specimens.
- In-plane diffraction on thin films.

X'Pert PRO utilizes the PreFIX concept that makes possible to perform more than one analysis on one system. PreFIX stands for: Pre-aligned Fast Interchangeable X-ray modules. The PreFIX concept enables diffraction systems to be reconfigured in a few minutes without the need for re-alignment to handle different types of analysis. The Philips X'pert diffractometer is made especially for materials analysis purposes. It is equipped with different pieces of optics for the incident beam and diffracted beam optics. By combining these optics a number of different types of analysis are available. The machine takes some practice to master, but it's Windows based software is brand new and quite user-friendly.

The X’pert PRO X-ray Diffraction system basically consists of the following

- Goniometer; the central part of the diffractometer.
- X-ray tube mounted onto the goniometer in a tube shield.
- Incident beam Optics and Diffracted beam optics.
- Sample stage on which a sample is mounted.
- A detector to measure the intensity of the X-ray Diffracted beam.

3.3 Goniometer:

The goniometer is the central part of the diffractometer. The standard resolution goniometer is used in X'pert PRO MPD systems.Generally the goniometer is a four-axis system with 2θ, θ, phi and psi as the variables. θ is the angle between the incident beam and the sample surface. It can be varied independently of 2θ, which is the angle between the incident beam and the diffracted beam. Phi is the rotation angle about the sample normal and Psi is the tilt angle about a horizontal and centered line in the sample surface: The goniometer used here is a two axis system with 2θ, θ as the variables.

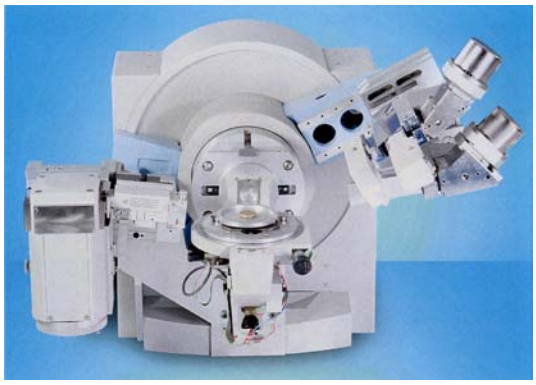

Figure 3.2 : Xpert PRO MPD(Multi Purpose Diffractometer) θ-2θ system (from Xpert manual)

Specifications: The goniometer has minimum θ and 2θ step sizes of 0.0001° and maximum step size of 1.27°.

The angular range of θ is -20° to 120° and of 2θ: - 40° to 170° .

The radius of the goniometer is in between 130mm-240mm.The actual radius of the Xpert PRO MPD system is 240mm.

3.3 X-ray Source:

The x-ray source used in the Xpert is a high power ceramic filament tube with a Cu-target. The filament is made of tungsten and can have maximum power of 2.2 kW, maximum voltage of 60kV and maximum current of 55mA. It is normally operated at 40 kV and 45 mA. Cu gives a K_α of 1.542 Å and K_β of 1.3922 Å. This is most commonly used for powder diffraction work with high resolution, phase identification and quantitative analysis.

Figure 3.3: Ceramic Diffraction X-ray Tube (from Xpert manual)

The tube can have either a point focus or a line focus. To switch between the two modes take approximately 5 minutes and no new alignment is necessary. The Focus type used for this tube is Line focus with 12mm x 0.4mm spot dimensions .The window diameter and thickness should be 14mm and 300µm.

3.5 Incident Beam Optics:

These are the primary optics placed in the line of the beam immediately after it leaves the tube housing.

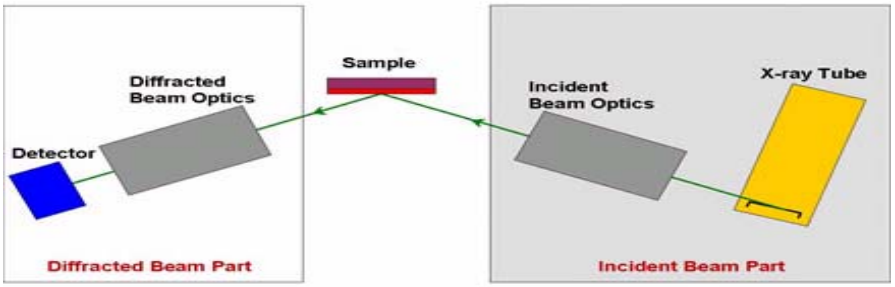

Figure 3.4: X-ray beam path leaving the incident beam part (from manual)

3.5.1 Programmable Divergence Slit (PDS):

Divergence slits are fitted in the incident beam path to control the equatorial divergence of the incident beam. The PreFIX programmable Divergence Slit is used in the incident beam path as shown in the figure.

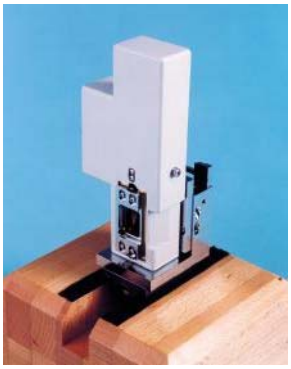

Figure 3.5: PW 3081/6x Programmable Divergence Slit (from Xpert manual)

This module incorporates a slot for beam Attenuation and filters, Soller slits and Beam mask holder. The Distance between the focus of the x-ray tube and divergence slit is 100mm. The divergence slit is software controlled to operate in two modes.

- Fixed divergence slit mode, to provide a defined divergence of 4°, 2°, 1/2°, 1/4°, 1/8°, 1/16° or 1/32°.
- The automatic divergence mode, to provide a defined irradiated length of 20 to 0.5 mm changing automatically as a function of θ.

In all the experiments performed for this report fixed mode was used with a divergence of 1/2°.

3.5.2 Incident Beam Mask :

Beam masks are fitted in the incident beam path to control the axial width of the incident beam, defining the amount (width) of the sample that is irradiated by the incident x-ray beam.

Figure 3.6: Incident Beam Masks (from Xpert manual)

The size of the beam mask opening must be such that the incident x-ray beam is completely accepted by the sample during the complete measurement. The total width of the area on the sample irradiated by the incident beam is dependent on the size of the x-ray beam and the position of the sample with respect to the beam. Four beam masks marked 5, 10,15 and 20 are supplied together with PDS as shown in the figure

above. The beam mask holder is mounted onto the programmable divergence slit so that the beam masks can be easily inserted and removed.

For all the experiments performed for this report incident beam mask of 15 mm was used.

3.5.2 Soller Slits:

When using a line source, radiation will emerge in directions both above and beneath the plane of incidence. To remove it, Soller slits are used. They consist of a set of closely spaced, thin metal plates parallel to the plane of the diffractometer circle. Using Soller slits improves the peak shape and the resolution in 2θ-type scans. Soller slits of 0.04 rad was used for all the experiments to limit the divergence to the diffractometer plane:

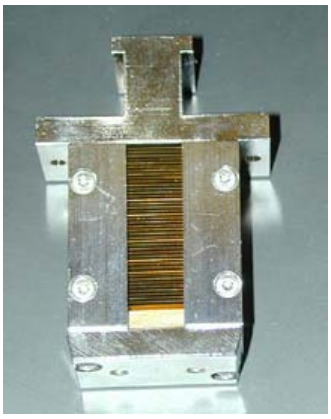

Figure 3.7: The 0.04 rad Soller slit (from Xpert manual)

3.6 Diffracted Beam Optics:

These are the secondary optics placed in the line of the beam immediately after the beam hits the sample and reflected. After leaving the secondary optics the reflected beam goes straight into the detector.

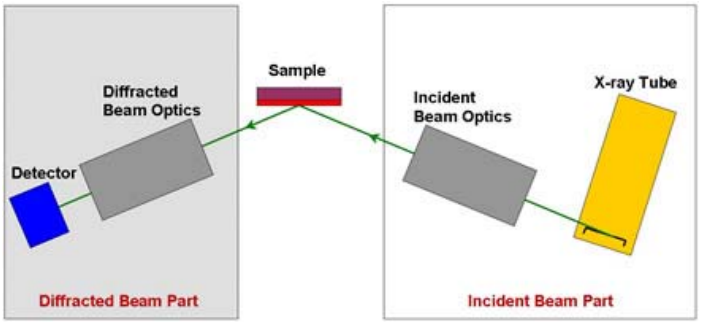

Figure 3.8: X-ray beam hitting the detector (from manual)

Slits used on the diffracted beam path can be divided into:

3.6.1. Programmable Receiving Slits (PRS):

The Programmable Receiving Slit is basically a slit that is programmable to optimize the intensity and resolution for the different experiments and it can be used with every primary optics other than the hybrid. The programmable receiving slit is used for stress and texture measurements and phase analysis. It has a diffracted beam crystal monochromator attached. Programmable Receiving Slit consists of a receiving slit unit as shown in the figure .It includes:

- A slot for Soller Slit
- A slot for Fixed Anti-Scatter Slit

- A slot for Crystal Monochromator

Figure 3.9: Programmable Receiving Slit with Fixed Anti Scatter Slit, Monochromator, Soller slit and detector (from Xpert manual)

The programmable receiving slit is software controlled to provide a defined receiving slit height, which can be varied between 0.01mm and 3.0mm. A receiving slit height of 0.1mm was used for all the experiments in this report.

3.6.2 Fixed Anti-Scatter Slit (FASS):

Only used for the Programmable Receiving Slit and only when the fixed slits are used. The antiscatter slits are used to reduce the amount of scatter that enters the secondary optics. They control the acceptance of the diffracted beam by the detector. Fixed Anti Scatter Slit can be mounted on the front of PRS. Five anti scatter slits marked 4°, 2°,1°,1/2° ,1/4 ° are used generally. A 1/2° FASS was used for all the experiments in this report.

3.6.3 Soller Slit:

Soller slits are used together with PRS to control the axial acceptance of the x-ray beam by the detector. Soller slits are mounted into the slot provided in the PRS as shown in the figure. These slits are inserted into the slot until it clicks into place. A size of 0.04 radians was used for all the experiments.

3.6.4. Curved Crystal Monochromator:

The monochromator is situated between the receiving optics and the detector. These monochromators are used to reduce the background radiation efficiently, eliminate unwanted lines such as K_β line completely and reduce the effect of sample fluorescence. Diffracted beam curved crystal monochromators are designed as single wavelength monochromators .The monochromator is aligned in away that ensures that only the required wavelength is collected by the detector. These can be only be mounted onto PRS.

3.7 Detector:

The x-ray detector is the last item in the x-ray beam path. X-ray detector is used to count the number of photons (intensity) of the diffracted beam at certain 2θ position of the goniometer. Xpert diffractometer uses sealed proportional detectors - sealed chambers filled with xenon/methane gas mixture. The detector is most efficient for Cu K_α radiation.

Figure 3.10: Proportional Detector (from Xpert manual)

The proportional detectors has the window size of 20 x 24 mm2 with Cu Kα efficiency of 84%, the energy resolution of 19 % and upto 1000 Kcps of maximum count rate there is 99 % linearity range in the counting

3.8 Sample Stage and Sample Holder:

Sample stage is a device onto which a sample is mounted so that it can be measured or analyzed. The sample stage used in the system is a PW 3071/60 stage for flat solids or powders in flat holders. This is used as an alignment shaft in the tube height alignment. It is mounted onto the X'Pert goniometer. The reference plane for the correct sample height is situated on the bottom surface of the surface clamp. The sample positioning height accuracy is + 10μm. A vertical reference line on the sample clamp indicates the symmetry plane of the sample stage.

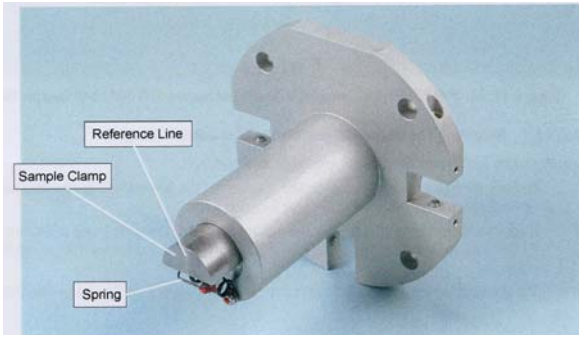

Figure 3.11: PW 3071/60 Sample Stage (from Xpert manual)

The sample holders are mounted on the sample holders. These are designed for the manually prepared powder samples. The powders are filled upto the top of the sample holders and leveled. The measurement range is from 0° 2θ upwards without obscuring the sample surface.

4. RESULTS

4.1 X-ray Diffraction Data:

Standard X-ray powder diffraction was performed on Fe_xNi_{100-x} powders for phase identification. X'Pert Data Collector software is used to collect the data from the powders supplied. The incident beam and diffracted beam optics used for the scans are same for all the samples. The incident beam part consists of x-ray tube and incident beam path. The x-ray tube is Cu K_α radiation of wavelength 1.54056 Å with a line focus having 12mm x 0.4mm spot dimensions was used. To control the equatorial divergence of the incident beam, a fixed divergence slit with a divergence of 1/2° was used. To control the axial width of the incident beam, a beam mask of 15 mm was used. Soller slit of 0.04 rad was used to limit the divergence of the radiation, since the radiation will emerge in directions both above and beneath the plane of incidence when using a line source. The diffracted beam optics consists of diffracted beam path and the detector. A fixed anti-scatter slit of 1/2° was used to reduce the amount of scatter that enters the diffracted beam optics. A soller slit of 0.04 rad was used to control the axial acceptance of the x-ray beam by the detector. A curved crystal monochromator is used to eliminate the unwanted radiation such as K_β and ensures only the required wavelength is collected by the detector. A detector is used to

count the number of photons (intensity) of the diffracted beam at certain 2θ position of the goniometer.

Scans were performed over a range of 2θ from 30°-120° with a step size of 0.05°, time per step of 25s for a total time of 14hrs. These parameters were obtained by conducting a quick scan over a bcc 110 peak of $Fe_{90}Ni_{10}$ sample. FWHM value of 0.4852 and 400 counts per sec was obtained. A minimum of 10 data points should be collected across the FWHM, so obtained FWHM/10 = 0.05 step size is selected resulting in good peak and a 25s time per step was used in order to get 10000 counts which is a very good counting statistics.

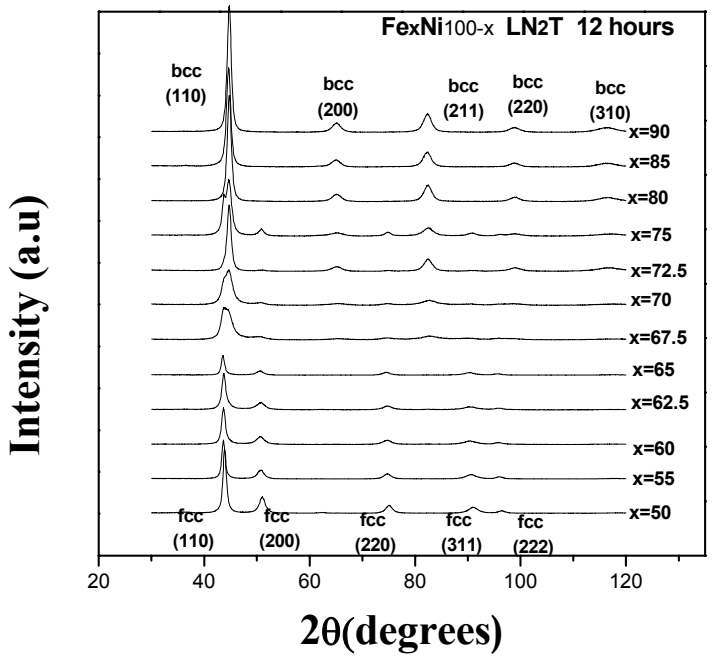

Figure 4.1: X-ray diffraction patterns from Fe_xNi_{100-x} alloys milled at liquid nitrogen temperature for 12 hours

Figure 4.1 presents X-ray diffraction patterns from ball milled powders of Fe_xNi_{100-x} where x = 90, 85, 80, 72.5, 75, 70, 67.5, 65, 62.5, 60, 55, 50. A transition can be followed from pure bcc structures at the iron rich compositions (x=90, 85, 80) to pure FCC structures at nickel rich compositions (x=62.5, 60, 55, 50). At intermediate compositions (x=72.5, 70, 65, 62.5) a two phase mixture of bcc and fcc structures is indicated. For $Fe_{75}Ni_{25}$ sample alloying did not occur and the diffraction pattern obtained is different from the transition observed. There should be a gradual change in the phase, but in the diffraction pattern of the $Fe_{75}Ni_{25}$ sample, it can be seen that the fcc (200) peak have more intensity than the other compositions in the two phase region. Therefore $Fe_{75}Ni_{25}$ sample will be excluded from the remainder analysis.

Figure 4.2 gives the X-ray diffraction patterns of the as received Fe powder and the ball milled $Fe_{90}Ni_{10}$ sample to show the broadening of the ball milled Fe peaks. This trend is observed in all the ball milled samples. The ideal peak of the pure Fe is very sharp and narrow and the observed peak profile of the ball milled samples broadens. The peak width of the pure iron is mainly due to instrumental broadening. The broadening in the ball milled samples is due to the structural imperfections such as finite crystallite size, lattice strain from mechanical deformation, stacking faults, micro twins etc.

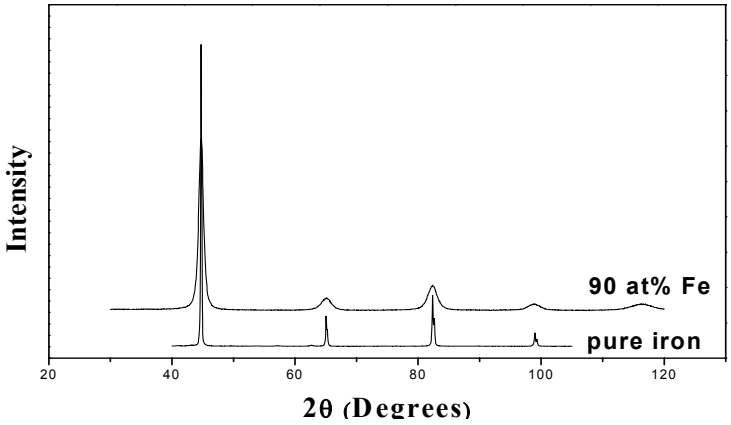

Figure 4.2: X-ray diffraction patterns of 90 at% Fe and pure Fe

In the following sections analysis, will be presented to quantify the phase fractions, estimate the lattice parameters and estimate the crystallite size.

4.2 Phase Fractions:

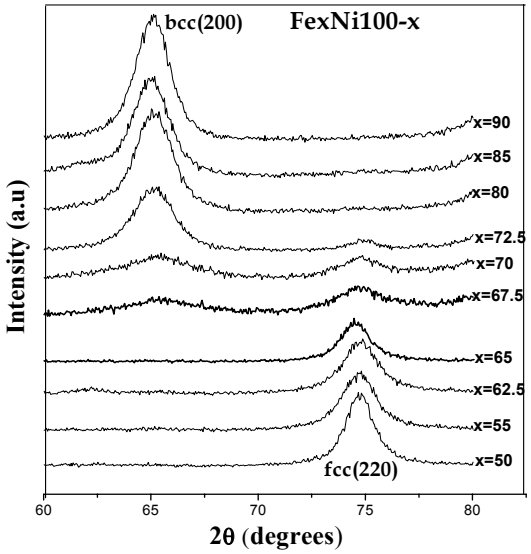

Figure 4.3: X-ray diffraction peak shapes of bcc(200) and fcc(220)

Phase fractions were obtained based on the relative intensities of bcc(200) and fcc(220). These peaks are shown in the Figure 4.3 and the intensities were assessed based on the integrated peak areas for a best fit (Lorentzian function). The peak areas were obtained from the X'Pert Highscore software, which is used to assess the peak parameters.

Several methods were used by the investigators to obtain the phase fractions. Xanes analysis technique was first used and tested on a set of Fe-Ni standard sample [Ref 52] and Cu-Fe samples [Ref 53]. The phase fractions determined by comparing the intensities of the bcc(200) and fcc(220) peaks after corrections for Lorentz polarization, multiplicity and structure factors in a similar manner is described by Hong and Fultz. In the method used in this research, phase fractions were obtained using a calibration curve. A series of standards were prepared using pure Fe as a bcc component and pure Ni as a fcc component. The powders were mixed to give the desired composition according to the atomic percentage. The mixtures with Ni (20, 40, 50, 60, 80) at% compositions were obtained. X-ray powder diffraction was performed on these powders using the same slits and scan parameters used earlier for the ball milled samples. Figure 4.4 gives the diffraction patterns of the prepared Fe_xNi_{100-x} powders.

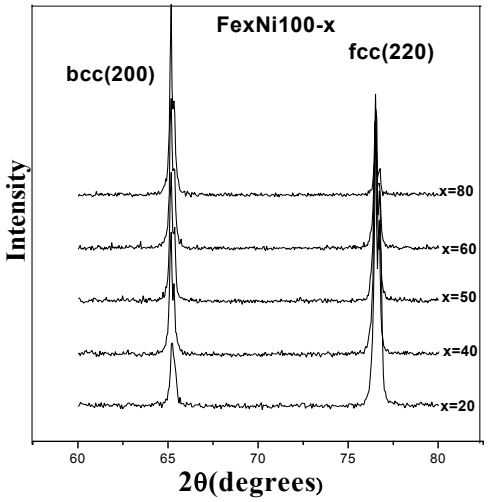

Figure 4.4: Diffraction patterns of bcc(200) and fcc(220) pure Fe_xNi_{100-x} (x = 80, 60, 40, 20)

$\%f_{fcc}$	$A_{fcc(220)}$	$A_{bcc(200)}$	A_{fcc220}/A_{bcc200}
0	-	-	0
20.01	35.97	112.6	0.242
39.87	107.01	129.01	0.453
49.85	174.07	109.1	0.615
60.01	204.52	124.57	0.621
80.01	312.8	66.2	0.825
100	-	-	1

Table 4.1: calculated peak areas, fractions of peaks areas and fcc phase

Tabe 4.1 gives the calculated peak areas, fractions of peak areas and fcc $A_{fcc220}/A_{bcc200+Afcc220}$ Vs $f_{fcc(220)}$ was plotted and a calibration curve is drawn.

Figure 4.5 shows the calibration curve. The curve plotted using the above values is a linear fit and the equation

$$\frac{A_{fcc(220)}}{A_{fcc(220)} + A_{bcc(200)}} = mf_{fcc} + b \text{ ---------- (15)}$$

is of the form y=mx+b , where m=0.00978 and b=0.01241. From the calibration curve it is observed that the peak area fraction is directly related to fcc phase fraction.

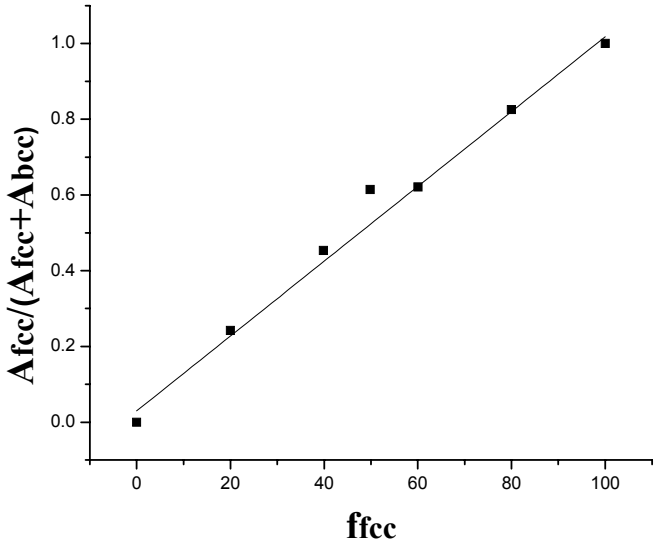

Figure 4.5: Calibration curve

Measured samples peak areas were obtained (see figure 4.3) and the peak areas fraction is calculated and the numbers are entered into the linear equation obtained by the curve fit and the % fcc phase fraction is calculated. Table 4.2 gives the phase fractions of fcc and bcc.

Ni at%	$A_{fcc(220)}$	$A_{bcc(200)}$	$A_{fcc220}/A_{bcc200+Afcc220}$	$\%f_{fcc(220)}$	$\%f_{bcc(200)}$
10	0	998.63	0	0	100
15	0	754.08	0	0	100
20	0	868.24	0	0	100
25	291	779	0.272	26.54	73.46
27.5	287.44	579	0.332	32.65	67.35
30	229.18	354	0.393	38.91	61.09
32.5	176.22	196	0.473	47.13	52.86
35	286.37	0	1	100	0
37.5	183.56	0	1	100	0
40	263.18	0	1	100	0
45	477.02	0	1	100	0
50	1130.12	0	1	100	0

Table 4.2: Measured peak areas, peak area fraction, % fcc and bcc phase fractions

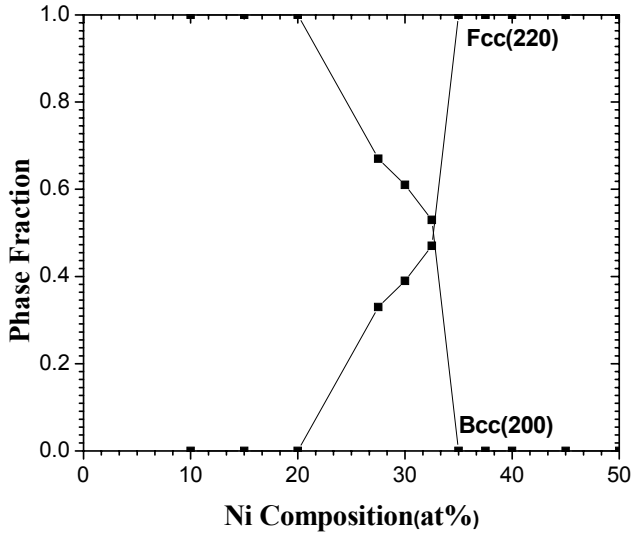

Figure 4.6: Fractions of bcc and fcc phases in as milled Fe_xNi_{100-x}

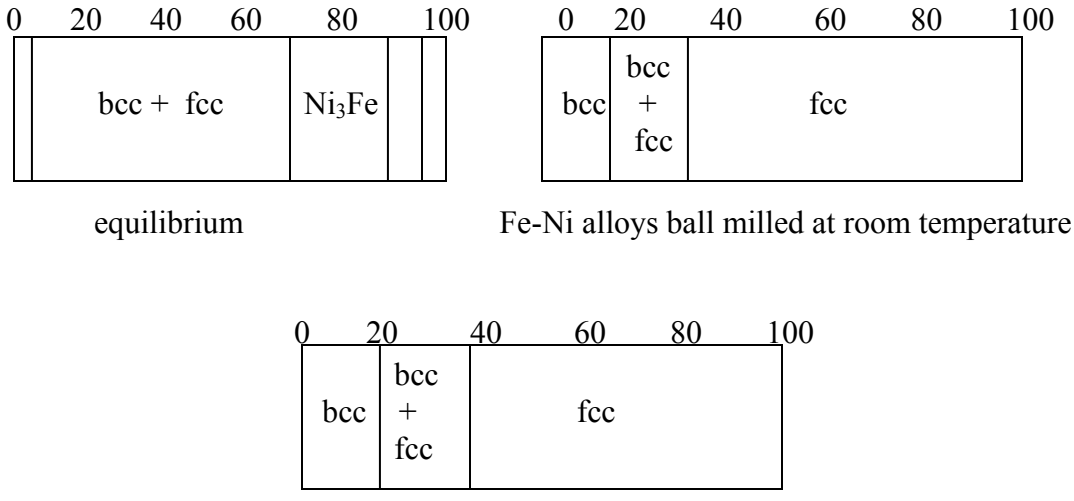

Figure 4.7: Phase boundaries for Fe-Ni alloys

The figure 4.6 gives the fractions of bcc and fcc phases. Figure 4.7 compares the phase boundaries of the bcc and fcc phases for Fe-Ni alloys at equilibrium, room temperature and low temperature. Thermodynamic equilibrium at room temperature shows a broad two-phase region, bounded on the right by $L1_2$ ordered Ni_3Fe which is based on fcc lattice. For Hong and Fultz ball milled Fe-Ni alloys at room temperature the two phase region is between 12 and 30 at% Ni and is shifted towards low Ni concentration. In comparison, with Hong and Fultz results, ball milled Fe-Ni alloys at liquid nitrogen temperature produce a two phase region between 20 and 37.5 at% Ni that is shifted towards high Ni-rich concentration.

4.3 Lattice Parameters:

The lattice parameters were determined using X'Pert Plus software by the unit cell refinement method which is done by the least squares fit method through the angular differences between measured peak and indexed reflections. Profile fitting is done before calculating lattice parameters. Profile fitting is used to extract better, more reliable peak parameters from the measured data .Only a limited number of peaks can be fitted at a time. So, for each sample, each peak is fitted and this generates a list of peak parameters. The results of profile fitting are the exact peak position, FWHM and the integral intensity.

The refinement is a straightforward least squares method using Levenberg-Marquard algorithm, which uses the observed Q-values. The cell parameters are refined and the standard deviations of the parameters are calculated. First all the possible reflections are generated starting either from some indexed reflections or from approximated cell parameters. Then the list of possible reflections is compared to the observed peaks and indices are assigned to the observed reflections within a given 2theta and intensity. From the d-values of the indexed observed lines new cell parameters are calculated. For the fcc phase 110, 200, 220, 311, and 222 peaks and for the bcc phase 110, 200, 211, 220, 310 peaks were used in a lattice parameter refinement. The lattice parameters of the unit cells are given in nanometers (nm) and are considered to accurate to ±2 in the last reported decimal.

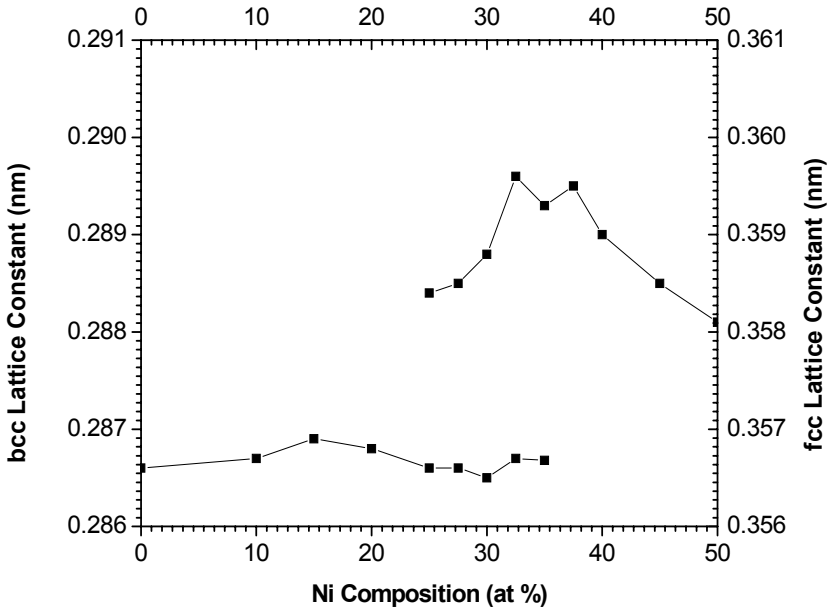

Figure 4.8 Lattice parameters of bcc and fcc phases in as milled Fe_xNi_{100-x} alloys

Figure 4.8 gives the lattice parameters of the bcc and fcc phases in as milled Fe_xNi_{100-x} alloys. From the graph it is evident that the bcc lattice parameters don't change in the Fe-rich compositions if the Ni is added. However, the fcc lattice parameter varies when Fe is added to the Ni compositions. According to the thermodynamic equilibrium, the composition of each phase in the two phase region is expected to be constant. The bcc lattice parameters in the composition of two phase region for the Fe-Ni samples ball milled at liquid nitrogen temperature remains constant. However, the lattice parameter of the fcc phase in the two phase region varies (from 3.584 to 3.596 Å). It indicates that the composition of the fcc phase varies in the two phase region. It is not constant as would be expected for a system in thermodynamic equilibrium. The lattice parameter of the bcc phase is insensitive to the chemical composition of the alloy, therefore a variation in the composition cannot be observed by x-ray diffraction

[Ref 49]. The results obtained were similar to the Hong and Fultz results observed in Fe-Ni samples ball milled at room temperature.

4.4 Crystallite Size:

X-ray diffraction is used to identify the crystalline phases, to analyze and to determine the composition, the size and the strain of the crystallites in the materials. Initially the peak is very sharp and broadens significantly due to the effects from *structural imperfections* such as finite crystallite size, lattice distortions, stacking faults and instrumental effects such as the diffractometer used to obtain the data, x-ray spectrum and the sample.

Various methods are employed to calculate the average crystallite size. The Integral breadth method using the Scherrer formula and Fourier methods are generally used to calculate the sources of peak broadening. To obtain the crystallite size, Scherrer formula is used in this research. The reason for the use of Scherrer method is because, Hong and Fultz used the same method on similar samples at room temperature and reported that the results from the Scherrer formula were consistent with the TEM (Transmission Electron Microscopy) observations of crystallite size. Data is collected for the bcc(211) phase and fcc(220) phase over a scan range of 70 - 80 for bcc(211) and 78-88 for fcc(220). The Full width half maximum (FWHM) is obtained from the peak parameters and using the FWHM of these peaks in the Scherrer method crystallite size is calculated.

$$L_{hkl} = \frac{K\lambda}{\beta \cos\theta} \text{----------(12)}$$

This is known as Scherrer's equation, where **K** is a Scherrer constant with a value $1.0 \geq K \geq 0.9$, **λ** is X-ray wavelength, **θ** is diffraction angle and **β** is integral breadth (in radians). Figure 4.9 shows the peak shapes of bcc(211) and fcc(220) of the as milled Fe_xNi_{100-x} plotted against Ni concentration. Table 4.3 gives the crystallite size of the bcc and fcc peaks.

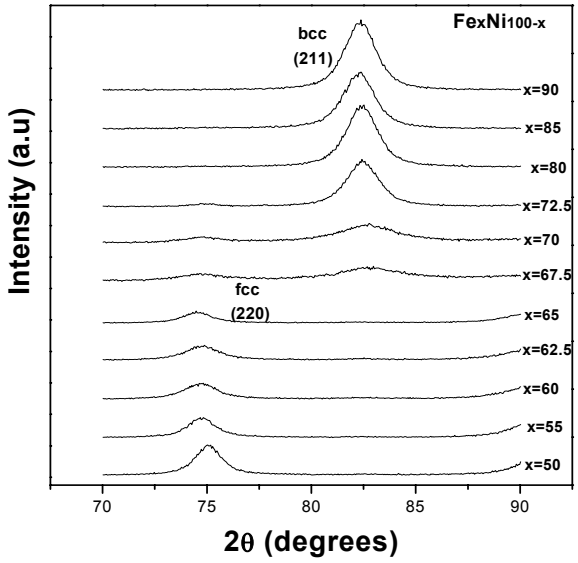

Figure 4.9 Peak shapes of bcc(211) and fcc(220) for crystallite size determination

Ni at%	FWHM(bcc 211)	FWHM(fcc 220)	Size	Size
10	1.702		6.895715	
15	1.721		6.813334	
20	1.68		6.985962	
27.5	1.726	1.357	6.798998	8.198355
30	2.771	1.792	4.240933	6.270368
32.5	3.025	2.141	3.88555	5.184637
35	0.242	1.516		7.317866
37.5		1.859		5.974699
40		1.683		6.596382
45		1.546		7.183798
50		1.395		7.974817

Table 4.3 Crystallite size values

Figure 4.10 shows the grain size of bcc(211) and fcc(200) phases plotted against Ni concentration. When compared to the Hong and Fultz results ball milled at room temperature, the grain sizes obtained for the samples in this research are smaller. In the case of Hong and Fultz results, the grain sizes of the ball milled Fe-Ni alloys at room temperature are greater than 10 nm. The fcc grain sizes(~ 15 nm) are much greater than the bcc(~ 10 nm) for the samples ball milled at room temperature. In comparison, the grain sizes obtained at liquid nitrogen temperature are much smaller and both the fcc and bcc crystallite sizes are approximately the same. This is due to the ball milling of Fe and Ni at the Liquid Nitrogen temperature, which makes the particles more brittle and more refinement is seen in the samples.

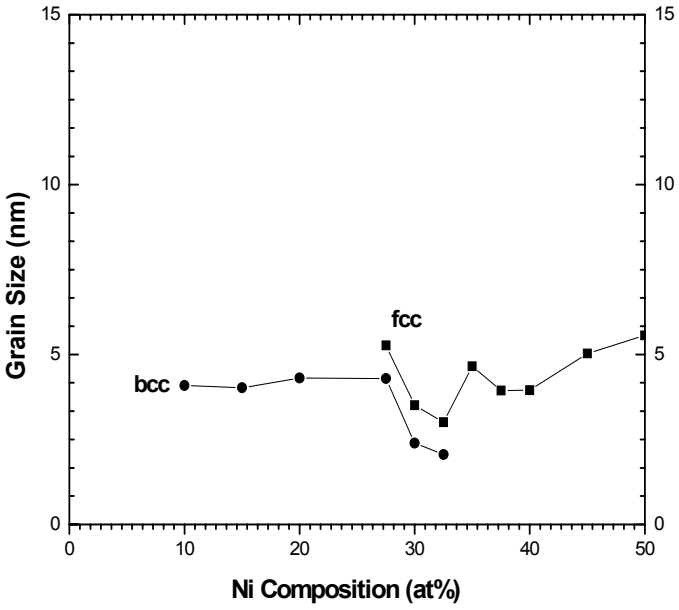

Figure 4.10 Grain size of bcc(211) and fcc(220) phases

5. CONCLUSIONS:

Mechanically alloyed Fe-Ni alloys over the range of x =100-50 were analyzed and phase fractions, lattice parameters and crystallite size were determined using X-ray powder diffraction. As discussed in the section 2.1.6 under synthesis of non-equilibrium phases, ball milling can cause many of the equilibrium and non-equilibrium phases. These include equilibrium and saturated solutions, stable and metastable crystalline intermediate phases, nanostructures and amorphous alloys. In the Fe-Ni system, it can be seen that these systems rapidly form nanostructures and solid solubility extensions.

It was found that the composition ranges of fcc and bcc single phase regions were greatly extended with respect to their equilibrium ranges. Figure 4.7 compares the phase boundaries of the bcc and fcc phases for ball milled Fe-Ni alloys at room temperature and low temperature with Fe-Ni alloys at equilibrium. Thermodynamic equilibrium shows a broad two-phase region, from 2 at% Ni to 71 at% Ni and bounded on the right by $L1_2$ ordered Ni_3Fe which is based on fcc lattice. For Hong and Fultz ball milled Fe-Ni alloys at room temperature the two phase region is between 12 and 30 at% Ni and is shifted towards low Ni concentration. In comparison, with Hong and Fultz results, ball milled Fe-Ni alloys at liquid nitrogen temperature produce a two phase region between 20 and 37.5 at% Ni that is shifted

towards high Ni-rich concentration. The ball milling extends the solubility of Ni in the bcc phase to at least 20 at% Ni and the Fe concentration in the fcc phase is extended to at least 62.5 at% Fe.

The bcc lattice parameters don't change in the Fe-rich compositions if the Ni is added. However, the fcc lattice parameter varies when Fe is added to the Ni compositions. The bcc lattice parameters in the composition of two phase region for the Fe-Ni samples ball milled at liquid nitrogen temperature remains constant. However, the lattice parameter of the fcc phase in the two phase region varies. It indicates that the composition of the fcc phase varies in the two phase region. The results obtained were similar to the Hong and Fultz results in samples observed at room temperature.

The grain sizes obtained for the Fe-Ni samples ball milled at liquid nitrogen temperature in this research are smaller when compared to the Hong and Fultz results ball milled at room temperature. In the case of Hong and Fultz results, the fcc grain sizes(~ 15 nm) are much greater than the bcc(~ 10 nm) for the samples ball milled at room temperature. The grain sizes obtained at liquid nitrogen temperature are much smaller and both the fcc and bcc crystallite sizes are approximately the same (~6nm). This is due to the ball milling of Fe and Ni at the Liquid Nitrogen temperature, which makes the particles more brittle and more refinement is seen in the samples.

REFERENCES

1. Powder Metallurgy – An Introduction by G Greetham

2. J S Benjamin- Material Science Eng, 1970, Vol .1, p.2943

3. J S Benjamin and P.S.Gilman1983 Ann.Rev.Mater.Sci. **13** 279

4. Benjamin J S. In:E Arzt and L Schultz *,"New Materials by Mechanical Alloying Techniques; Mechanical Alloying –A Perspective",* 1989; p.3-18.

5. H K D H Bhadeshia*, "Recrystallisation of practical mechanically alloyed iron-base and nickel-base superalloys"*, Mater.Sci.Eng. A **223 ,** 64 (1997).

6. E.Hellstern, H.J.Fecht, Z.Fu and W.L.Johnson, *"Nanocrystalline metals prepared by High Energy Ball Milling"*,Metall. Trans. A, Phys. Metall. Mater. Sci. (USA) **21A** (Sept. 1990) 2333-7.

7. C.Suryanarayana, *"Mechanical Alloying and Milling"*, Progress in Material Science, 46(2001) 1-184.

8. Lee w, Kwun SI, Journal of Alloys and Compounds,1996;240:193-9.

9. Calka A, Nikolov JI, Ninham BW, In:deBarbadillo JJ,et al., editors. *"Mechnical alloying for structural applications"*;1993 .p.189-95.

10. Suryanarayana C, Chen GH, Froes FH, **"***Nanostructure processing for Titanium- based materials"*, Scripta Metall Mater, 1992; **26**; 1727-32.

11. Hong LB, Bansal C, Fultz B, *"Steady state grain size and thermal stability of nanophase Ni_3Fe and Fe_3X (X = Si, Zn, Sn) synthesized by ball milling at elevated temperatures"***,** Nanostructured materials, 1994; **4**, 949-56.

12. Koch CC, *"The synthesis and structure of nanocrystalline materials produced by mechanical attrition: A review",* Nanostructured materials,1993; **2** : 109-29.

13. Suryanarayana C, International Materials review ,1995; **40** : 41-64.

14. C Capdevilla, Y L Chen, A R Jones, and H K D H Bhadeshia, *"Grain Boundary Mobility in Fe-Base Oxide Dispersion Strengthened Alloy",* ISIJ International, Vol. 43(2003), No.5, pp. 777-783.

15. E Ivanov and C Suryanarayana, "*Materials and Process Design through Mechanochemical routes*", Journal of Material Synthesis and Processing, **8**, 235 – 244 (2000)**.**

16. He, J H, H W Sheng, J S Lin, P J Schilling, R C Tittsworth and E Ma, *" Homogeneity of a Supersaturated Solid Solution",* Phys. Rev. Lett. **89** (2002): 125507.

17. T F Grigorieva, A P Barinova, V V Boldyrev, E Y Ivanov, *"The Solubility Limit and Mechanical Alloying process in Ni-X, Cu-X (X=Ge,Ga, Al, In, Sn) Systems",* Materials Sci.Forum,Vols.225-277 (1996) pp. 417-422

18. R B Schwarz, R R Petrich, C R Saw, J. Non-Cryst.Solids, **76**,281 (1985)

19. Murthy B S, Mohan Rao M and Ragnathan S, *"Nanocrystalline phase formation and extension of solid solubility by mechanical alloying in Ti-based systems",* Nanostructured Mater., **3**, 459 (1993).

20. Zhou E, Suryanarayana C, Froes FH, Mater.Lett., **23**, 27(1995).

21. K Uenishi, K F Kobayashi, K N Ishihara and P H Shingu, *"Formation of a super-saturated solid solution in the Ag---Cu system by mechanical alloying",* Mater.Sci.Eng. A **134**, 1342 (1991).

22. K Uenishi, K F Kobayashi, S Nasu, H Hatano, K N Ishihara and P H Shingu, Z.Metallkd. 83, **132** (1992).

23. A R Yavari, P J Desre and T Benameur, *"Mechanically Driven Alloying of Immiscible Elements"*, Phys. Rev. Lett. **68**, 2235 (1992).

24. C Gente, M Oehring and R Bormann, *"Formation of thermodynamically unstable solid solutions in the Cu-Co system by mechanical alloying"*, Phys. Rev. B **48**, 13244 (1993).

25. E Gaffet, C Louison, M Harmelin and F Faudot, *"Metastable phase transformations induced by ball-milling in the Cu---W system"*, Mater.Sci.Eng. A **134**, 1380 (1991).

26. F Fukunaga, M Mori, K Inou and U Mizutani, *"Amorphization in an immiscible Cu---V system by mechanical alloying and structure observed by neutron diffraction* ", Mater.Sci.Eng. A **134**, 863 (1991).

27. K Sakurai, Y Yamada, C H Lee, T Fukunaga and U Mizutani, *"Solid state amorphization in the Cu---Ta alloy system"* , Mater.Sci.Eng. A **134**, 1414 (1991).

28. K Sumiyama, K Yanai, E Ivanov, H Yamuchi and K Suzuki, *"Non-equilibrium phase formation and valence fluctuation in immiscible Ce---Yb alloys produced by mechanical milling and sputtering"*, Mater.Sci.Eng. A **181/182**, 1268 (1994).

29. E Ma, J H He and P J Schilling, *"Mechanically alloying of immiscible elements : Ag-Fe contrasted with Cu-Fe"*, Phys. Rev. B **55**, 5542 (1997).

30. J Xu, U Herr, T Klassen and R S Averback, *"Formation of supersaturated solid solutions in the immiscible Ni-Ag system by mechanical alloying"*, J. Appl. Phys. **79** (8), 3935, 1996.

31. Eckert J, Schultz L and Urban K, *"Formation of quasicrystals by mechanical alloying"*, Appl.Phys.Lett., **55**,117 (1989).

32. Koch CC, J S C Jang and P Y Lee. In:E Arzt and L Schultz *,"New Materials by Mechanical Alloying Techniques; ",* 1989; p.101-110.

33. Chitralekha J, Raviprasad K, Gopal E S R and Chattopadhyay K, J. Mater. Res., **10**, 1897 (1995)

34. L Lu, M O LAl and S Zhang, *"Fabrication of Ni3Al Intermetallic Compound Using Mechanical Alloying Technique",* Journal of Mater.Proc.Tech **48**, (1995) 683-690.

35. Bakker H, Zhou G F, Yang H," *Mechanically driven disorder and phase transformations in alloys",* Prog.Mater.Sci., **39**, 159 (1995a).

36. Cho Y S and Koch CC, J. Alloys & Compounds, **194**, 287 (1993).

37. C N Chinnaswamy, A Narayanaswamy, N Ponpandian, K Chattopadhyay, M Saravanakumar, *"Order-disorder studies and magnetic properties of mechanically alloyed nanocrystalline Ni_3Al alloy",* Mater.Sci.Eng A **304-306**, (2001) 408-421.

38. Jang J S C and Koch C C, J. Mater. Res., **5**, 498 (1990).

39. Seki Y and Johnson W L, "Solid State Processing", p. 287 (1990)

40. C Suryanarayana, "Non-Equilibrium Processing of Materials", **Vol 2**, (1999).

41. Weeber A W and Bakker H, Physica B, **153**, 93 (1988).

42. Koch CC, Cavin OB, McKmey CG and Scarbourgh JO, Appl.Phys.Lett. **43**, 1017 (1983).

43. R B Schwarz and W L Johnson, Phys.Rev.Lett. **Vol 51**, (1983), pp. 415-18.

44. E Hellstern and L Schultz, Appl.Phys.Lett. **49**, (1986), pp.1163-65.

45. B S Murthy, *" Mechanical alloying – a novel synthesis route for amorphous phases"*, Bull.Mater.Sci. **Vol 16,** (1993), pp. 1-17.

46. B L Chu, C C Chen and T P Perng, *"Amorphization of $Ti_{1-x}Mn_x$ Binary Alloys by Mechanical Alloying",* Metal.Trans **23A***,* 2105 (1992).

47. E Hellstern and L Schultz, Phil. Mag. 56, **Vol 56**, (1987), pp. 443-50.

48. Christian N J Wagner and Michael S Boldrick, *"The structure of amorphous binary metal-metal alloys prepared by mechanical aloyying",* J.Alloys & Compounds, **194**, 295-302 (1993).

49. Hong L B and Fultz B, *J. Apply. Phys*., 1996,79, 3946.

50. Hong L B and Fultz B, *Acta. matter*., 1998,46, 2937.

51. G K Williamson and W H Hall, *Acta. Metall.* **1**, 22(1953)

52. C Kuhrt and L Schultz , *J. Apply. Phys.* **73**, (1993) 1975.

53. C Kuhrt and L Schultz , *J. Apply. Phys.* **73**, (1993) 6588.

54. Yu V Baldokin, V V Teherdyntsev, S D Kaloshkin, G A Kochetov, Yu A Postov, *J. Magn. Magn. Mater.* **203**, (1999) 313.

55. S D Kaloshkin, V V Tcherdynstev, I A Tomilin, Yu V Baldokin, E V Shelekhov, *Physica B* **299**, (2001) 236-241.

56. R Jenkins and Robert L Snyder, *"Introduction to X-ray Powder Diffractometry"*, (1996) pp. 64 – 75.

57. "Production of X-rays and Interactions of X-rays with Matter",Goaz and Pharoah. Pages 11-20.

58. W.L.Bragg, Proc.Cambridge Phil.Soc., 17, 43 (1913).

59. P.P.Ewald, Handbuch der Physik, Julius Springer, Berlin, 1927, vol. XXIV, pp 191-369.

60. R Jenkins and Robert L Snyder, *"Introduction to X-ray Powder Diffractometry"*, (1996) pp. 64 – 75.

61. Klug H P and Alexander L E, "X-Ray Diffraction Procedures", 2nd ed., 1974.

62. Cullity B D , "Elements of X-ray Diffraction, 2nd ed., 1978.

63. *"X'Pert PRO User's Guide"* ,3rd edition, PANalytical B.V.

VITA

The author was born on 6th April, 1978 in Hyderabad, India. He completed his high school studies from N.S.K.K High School, Hyderabad, India. He joined Nagarjuna University, Vijayawada, India for Bachelor's degree in Mechanical Engineering in August 1996 and earned his degree in June 2000. He did his master's in Mechanical Engineering at University of New Orleans and graduated in December , 2003